Lithos 320–321 (2018) 1–19

Contents lists available at ScienceDirect

Lithos

journal homepage: www.elsevier.com/locate/lithos

Yttrium-zoning in garnet and stability of allanite in metapelites from the Main Central Thrust Zone and adjacent higher Himalayan crystallines along the Alaknanda Valley, NW Himalaya

S.S. Thakur [a,*], K. Madhavan [b], S.C. Patel [b], D. Rameshwar Rao [a], A.K. Singh [a], S. Pandey [a], P. Nandini [c]

[a] Wadia Institute of Himalayan Geology, 33 GMS Road, Dehradun 248001, India
[b] Department of Earth Sciences, Indian Institute of Technology Bombay, Powai, Mumbai 400076, India
[c] Central University of Karnataka, Kalaburagi, 585367, India

ARTICLE INFO

Article history:
Received 22 March 2018
Accepted 2 September 2018
Available online 5 September 2018

Keywords:
Garnet zoning
Allanite
Yttrium
Main Central Thrust Zone
Himalaya

ABSTRACT

Yttrium (Y)zoning in garnet and the stability of accessory allanite in metapelites from a greenschist to amphibolite facies inverted metamorphic sequence in the Main Central Thrust Zone (MCTZ) and the overlying Higher Himalayan Crystalline Sequence (HHCS) along the Alaknanda Valley in NW Himalaya have been studied. Garnet porphyroblasts from the garnet grade MCTZ metapelites commonly show chemical zoning with a Y-rich core (~3311 ppm) and Y-poor rim (b.d.). Phase diagram modelling for an MCTZ sample shows that the garnet zoning developed during prograde metamorphism in the *P–T* ranges of ~5.3–7.3 kbar and ~500–585 °C. Accessory allanite (up to 3.45 wt% Y_2O_3) occurs as inclusion in the rim of garnet porphyroblasts and also in the matrix in most of the MCTZ samples. The Y depletion in the rim of zoned garnets from the MCTZ has possibly resulted from sequestration of Y by allanite, which became a stable phase after the formation of the garnet core. Alternatively, the Y zoning has developed by strong partitioning of the element into garnet with the result that it is mostly incorporated in a narrow core and there is little Y available towards the later part of garnet growth. High-Y annulus occurs in a relatively inclusion-free zone of garnet porphyroblast from an MCTZ rock which has likely developed due to a decrease in the growth rate of the crystal. A garnet from the HHCS metapelites with localised resorption of the rim exhibits weak Y zoning marked by a slight increase in Y at the rim which is attributed to back-diffusion of the element during resorption. With increasing structural level across the MCTZ, the ΣLREE content of allanite first increases then decreases which is complemented by variation in the Al content of the mineral. This compositional variation of allanite appears to be linked to the modal abundance of garnet in rocks.

1. Introduction

Garnet is one of the important rock-forming and porphyroblast-forming minerals which under favourable metamorphic conditions sequesters yttrium (Y^{3+}) in its crystal structure during metamorphic growth. Different patterns of Y zoning in garnet and partitioning of the element relative to accessory phases such as monazite and allanite in metapelites have been studied by several workers (Corrie and Kohn, 2008; Groppo et al., 2010; Hermann and Rubatto, 2003; Kohn, 2004; Kohn and Malloy, 2004; Lanzirotti, 1995; Pyle and Spear, 1999, 2003; Regis et al., 2014; Shrestha et al., 2017; Spear and Kohn, 1996; Wang et al., 2015; Yang and Pattison, 2006). In spite of the occurrence of Y as a trace element in garnet, its slower diffusivity compared to the major divalent cations (Fe, Mg, Mn and Ca) favours the retention of Y-zoning patterns even at high-grade metamorphic conditions (Lanzirotti, 1995; Hermann and Rubatto, 2003). This is the reason that Y is considered as one of the best tracers to study garnet zoning. Such studies are important in understanding the *P–T* evolution of metamorphic rocks and in monitoring the participation of Y-bearing accessory phases such as allanite (LREE epidote), monazite (LREE phosphate) and xenotime (Y phosphate) in metamorphic reactions. Furthermore, monazite and allanite are known as important geochronometers (Engi, 2017; Yakymchuk et al., 2017 and references therein). They have great implications on the dating of metamorphic events, and in turn, deciphering the tectono-metamorphic evolution (*P–T–t* path) of orogenic belts.

Despite various efforts over the past decade, the metamorphic conditions under which allanite forms relative to monazite in pelites are not precisely understood. Several workers have suggested that allanite formation is favoured in lower metamorphic grade rocks, whereas monazite is stable at higher metamorphic grades (Catlos et al., 2002; Fraser

* Corresponding author.
E-mail address: satya_edu1974@yahoo.co.in (S.S. Thakur).

https://doi.org/10.1016/j.lithos.2018.09.002
0024-4937/

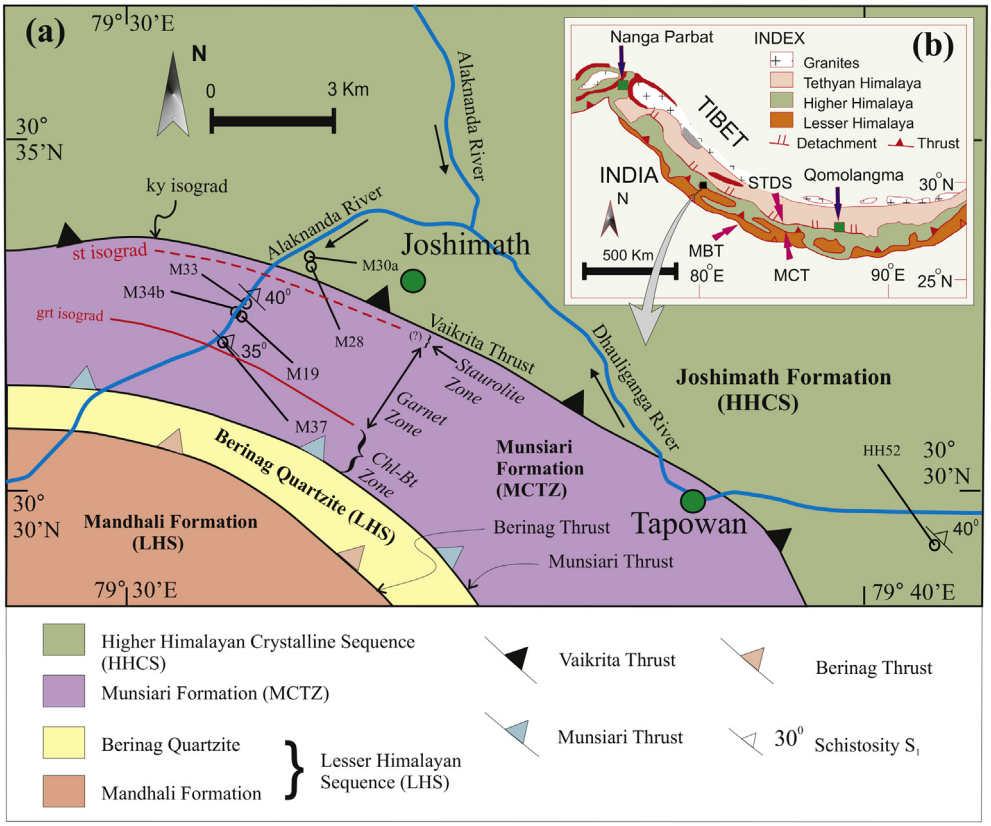

Fig.1. (a)Geological map of Alaknanda Valley modified after Valdiya (1980), Celerier et al. (2009) and Thakur et al. (2015). Sample locations are marked by black circles. Inset (b)shows a regional map of the Himalayan orogen. The location of St isograd is inferred from Gururajan and Choudhuri (1999) and Spencer et al. (2012). Metamorphic zones in the MCTZ are after Gururajan and Choudhuri (1999), Spencer et al. (2012) and Thakur et al. (2015). Abbreviations: HHCS = Higher Himalayan Crystalline Sequence; LHS = Lesser Himalayan Sequence; MCTZ = Main Central Thrust Zone.

et al., 2004; Gasser et al., 2012; Goswami-Banerjee and Robyr, 2015; Janots et al., 2006; Krenn and Finger, 2007; Rasmussen et al., 2006; Smith and Barreiro, 1990; Spear, 2010; Tomkins and Pattison, 2007; Wing et al., 2003). Nonetheless, there is little agreement among researchers on whether monazite occurs as a detrital phase (Ferry, 2000; Janots et al., 2008; Krenn et al., 2008; Suzuki and Adachi, 1994) or a metamorphic phase at amphibole and granulite grade conditions (Heinrich et al., 1997; Townsend et al., 2000; Catlos et al., 2001; Wing et al., 2003; Finger et al., 2016). Some other studies have emphasized the influence of bulk rock composition on the stability of allanite and monazite (Janots et al., 2007; Spear, 2010; Wing et al., 2003). Various metamorphic reactions involving accessory phases (such as allanite and monazite) and major phases (such as Y-bearing zoned garnet) have been suggested by many researchers on the basis of mineral chemistry and textural relation (Janots et al., 2008; Kohn and Malloy, 2004; Pyle and Spear, 2003; Spear, 2010; Wing et al., 2003; Yang and Pattison, 2006), and thermodynamic considerations (e.g. Corrie and Kohn, 2008; Janots et al., 2007; Spear, 2010). Trace element zoning in garnet has been attributed to a number of processes including Rayleigh fractionation (Baxter et al., 2017; Hollister, 1966; Otamendi et al., 2002), diffusion-limited uptake (Baxter et al., 2017; Moore et al., 2013; Skora et al., 2006), incorporation governed by partitioning with major phases involved in garnet-forming reactions (Konrad-Schmolke et al., 2008), and to partitioning with changing accessory phase assemblages (Cruz-Uribe et al., 2015; Dragovic et al., 2016; Hickmott and Spear, 1992; Moore et al., 2013; Pyle and Spear, 1999; Yang and Pattison, 2006). These processes give rise to various types of Y zoning in garnet including concentric zoning, sector zoning, oscillatory zoning and spiral zoning (Hickmott and Spear, 1992; Kohn and Malloy, 2004; Martin, 2009; Pyle and Spear, 1999).

While there are several reports of Y zoning in pelitic garnet from the central Himalaya (Groppo et al., 2010; Kohn, 2004; Martin, 2009; Shrestha et al., 2017; Wang et al., 2015), only a few studies are available from the eastern Himalaya (Mottram et al., 2015; Regis et al., 2014, 2016) and NW Himalaya (Caddick et al., 2007; Langille et al., 2012). Goswami-Banerjee and Robyr (2015) discussed the stability of monazite and allanite in pelites from the Miyar Valley in the NW Himalaya but did not address Y zoning in garnet. The study of Y zoning is important in understanding the metamorphic history and the growth/consumption of Y-bearing accessory phases during metamorphic reactions. In keeping with this view, a detailed metamorphic study has been carried out on pelites from the Main Central Thrust Zone (MCTZ) and Higher Himalayan Crystalline Sequence (HHCS) along the Alaknanda Valley, NW Himalaya. The study focuses on Y zoning in garnet and investigates the compositional variation of Y-bearing allanite under metamorphic conditions ranging from greenschist to amphibolite facies.

2. Geological background

The Himalayan Orogenic Belt, a classic example of a young mountain chain on earth, has resulted from Cenozoic continent-continent collision and is comprised of four lithotectonic units from south to north: the Sub-Himalaya, the Lesser Himalayan Sequence (LHS), the Higher Himalayan Crystalline Sequence (HHCS) and the Tethys Himalayan Sequence (THS) (Gansser, 1964; Hodges, 2000; Kohn, 2014; Lefort, 1975; Valdiya, 1980; Yin, 2006). The lithotectonic units are separated from each other by discrete continental scale thrust/normal faults (Fig.1). Starting from the south, the Sub-Himalaya, a Mio-Pliocene sedimentary package of the Siwalik Group is separated from the LHS of unmetamorphosed to

Table1
Mineral assemblages and *P–T* conditions of metamorphism of MCTZ and HHCS rocks from the Alaknanda Valley (after Thakur et al., 2015) (*T* in °C and *P* in kbar).

Sample	Mineral assemblage	Major element zoning in garnet	Metamorphic zone	Occurrence of allanite and monazite	Av. P-T Method*		Isopleth thermobarometry**	
					Core	rim	core	rim
MCTZ samples								
M37	grt-chl-bt-ms-pl-qz-ilm-tur-aln	Garnet porphyroblast is chemically zonned. The X_{sps} and X_{grs} content decrease from core to rim which is balanced by increase in X_{prp} and X_{alm}.	Garnet zone	Allanite and monazite present in the matrix. They did not observe as inclusion in the garnet porphyroblast.	569 ± 14 (8.6 ± 0.9)	579 ± 14 (8.1 ± 0.9)	577 (7.3)	–
M19	grt-chl-bt-ms-pl-qz-ilm-tur-aln	Garnet porphyroblast is chemically zonned. The X_{sps} content decreases from core to rim which is balanced by an increase in $X_{prp.}$ The X_{alm} content fluctuates from core to rim which is complemented by variation in $X_{grs.}$	Garnet zone	Allanite occurs as inclusion in the garnet as well as in the matrix. Monazite is present in the matrix only.	567 ± 14 (8.5 ± 0.8)	578 ± 14 (9.0 ± 0.8)	560 (7.0)	582 (7.5)
M34B	grt-chl-bt-ms-pl-qz-ilm-tur-aln	Garnet porphyroblast is chemically zonned. The X_{sps} decreases from core to rim whereas X_{prp} increases. The X_{grs} and X_{alm} content remain nearly uniform through out the grain.	Garnet zone	Allanite occurs as inclusion in the garnet as well as in the matrix. Monazite is absent in the sample.	569 ± 15 (7.7 ± 0.9)	586 ± 14 (8.2 ± 0.8)	550 (6.3)	593 (7.5)
M33	grt-chl-bt-ms-pl-qz-ilm-tur-aln	Garnet porphyroblast shows feeble chemical zoning. The X_{sps} and X_{grs} content decrease from core to rim whereas X_{prp} and X_{alm} content decrease.#	Garnet zone	Allanite occurs as inclusion in the garnet as well as in the matrix. Monazite is absent in the sample.	586 ± 14 (8.0 ± 0.8)	–	566 (6.5)#	576 (6.6)#
HHCS samples								
M28	grt-ky-bt-ms-pl-qz-ilm-rt-aln	Garnet porphyroblast is broadly chemically homogeneous with a very thin Mn-rich rim.	Kyanite zone	Allanite occurs as inclusion in the garnet as well as in the matrix. Monazite is absent in the sample.	708 ± 30 (11.9 ± 1.4)	–	–	–
HH52	grt-ky-bt-ms-pl-qz-ilm	Garnet is chemically homogeneous.	Kyanite zone	Monazite occurs as a matrix phase. Allanite is absent in the sample.	659 ± 25 (9.5 ± 1.3)	–	610 (8.0)	–

**Error bars are ±50 °C and ± 1 kbar (Palin et al., 2016 and references therein).
* The mineral assemblage used in *P–T* calculation for MCTZ samples is grt-bt-chl-ms-pl-qz and for HHCS samples is grt-ky-bt-ms-pl-qz.
# From this study.

low-grade metasedimentary rocks of Palaeo- to Mesoproterozoic age in the north by a north dipping thrust fault, called the Main Boundary Thrust. The LHS is separated from the HHCS by a thrust fault known as Main Central Thrust Zone (MCTZ). The MCTZ is a large scale high strain zone of distributed deformation and is believed to have juxtaposed the medium to high-gradeHHCS rocks of Neoproterozoic to Cambrian age to north over the LHS in the south (Robinson et al., 2003; Searle et al., 2008; Thakur et al., 2015). Moving further north, the HHCS is separated from the THS by the South Tibetan Detachment System, which is a network of north dipping, top-to-north, normal sense detachment faults.

The MCTZ in the Alaknanda Valley, NW Himalaya is a 3–4 km thick sequence of sheared metasedimentary rocks that occur between the HHCS in the north and the LHS in the south (Celerier et al., 2009; Hodges and Silverberg, 1988; Spencer et al., 2012; Thakur et al., 2015; Valdiya, 1980) (Fig.1). In this valley, the upper boundary of the MCTZ is marked by the Vaikrita thrust (MCT-II of Arita, 1983), which coincides with the kyanite-in isograd in the overlying HHCS(Thakur et al., 2015). The base of the MCTZ is marked by the Munsiary Thrust (MCT-I of Arita, 1983), which separates the MCTZ from the underlying LHS.

The dominant lithologies of the MCTZ in the Alaknanda Valley are garnet mica-schist/phyllite, quartzite, and hornblende schist with local lenses of calc-silicate rocks (Gururajan and Choudhuri, 1999; Thakur et al., 2015). The bedding in the MCTZ rocks is transposed to the prominent schistosity with dips ranging from ~30° to ~45° towards northeast. Shear sense criteria indicate top–to–southwest sense of shearing. The metamorphic sequence in the MCTZ is inverted with increasing grade from chlorite-biotite grade at the lower structural level to staurolite grade at the upper structural level. Thakur et al. (2015) did not observe staurolite in their MCTZ samples and described the whole upper MCTZ section as garnet grade rocks. However, its occurrence in the upper part of the MCTZ has been reported by Gururajan

Table2
Modal abundance of minerals (in percent) in the MCTZ and HHCS rocks based on visual estimation in thin sections (after Thakur et al., 2015).

Mineral	grt	chl	bt	ms	ky	pl	qz	opq	tur	aln
MCTZ sample										
M37	5	1	10	30	0	13	40	1	1	<<1
M19	8	3	7	12	0	16	50	1	<1	<<1
M34B	15	1	5	25	0	<1	50	1	1	<<1
M33	7	1	3	20	0	2	65	2	<1	<<1
HHCS sample										
M28	5	0	22	6	<1	12	54	1	0	<<1
HH52	7	0	19	16	<1	4	50	2	0	0

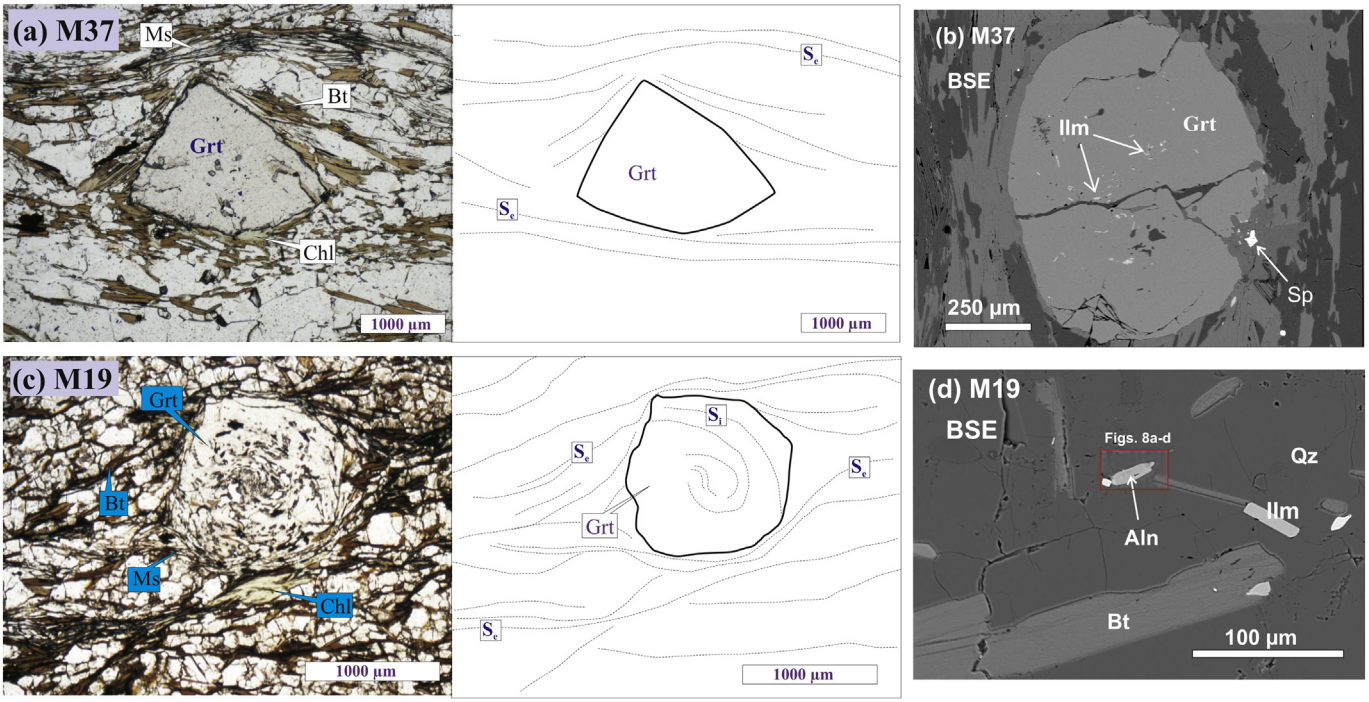

Fig. 2. Photomicrographs and corresponding line drawings (a, c) and BSE images (b, d) of MCTZ samples. (a) Warping of external foliation (S_e) around inclusion-free garnet porphyroblast (sample M37; plane polarised light); (b) Garnet porphyroblast with ilmenite inclusions. Note a sphalerite grain near garnet porphyroblast; (c) Snowball type S_i pattern in garnet (sample M19; plane polarised light); (d) elongated allanite grain in the matrix aligned parallel to the main foliation (sample M19).

and Choudhuri (1999) and Spencer et al. (2012) which indicates the influence of bulk-rock composition on the appearance of staurolite. Garnet growth has been interpreted to be *syn*-kinematic with the shearing event in the MCTZ(Moharana et al., 2013; Thakur et al., 2015). However, the temporal relation between the shearing deformation and garnet growth in the MCTZ is debated in various sections of the Himalayan orogen (Kohn et al., 2001; Yin, 2006 and references therein). Peak metamorphic *P–T* conditions of 550–593 °C and 6.3–7.5 kbar for the garnet grade MCTZ rocks, and 610–708 °C and 8.0–11.9 kbar for the basal part of the kyanite grade HHCS rocks have been reported by Thakur et al. (2015)(Table1). The *P–T* estimates calculated using Av. P-T method for Alaknanda Valley samples are slightly higher than those obtained from the isopleth method, but the values from the two methods are mostly similar within error limits.

3. Petrography

Four MCTZ samples (M37, M19, M33, M34B) and two HHCS samples (M28, HH52), which were studied by Thakur et al. (2015), have been investigated in the present study. Salient petrographic features and the nature of occurrence of allanite and monazite in the samples are presented in Table1. Modal abundances of minerals estimated on polished thin sections using the optical microscope are given in Table2. Mineral abbreviations used in the text, tables and figures are from Whitney and Evans (2010).

3.1. MCTZ rocks

3.1.1. General characteristics

The MCTZ rocks are chlorite–biotite-bearing at lower structural levels, while garnet appears at higher structural levels. The rocks exhibit a dominant shear foliation (S_1) defined by the alignment of phyllosilicate minerals such as biotite and muscovite. Garnet occurs as subhedral to anhedral porphyroblasts of ~500–3600 µm diameter which are commonly wrapped by the matrix foliation. Most of the garnet porphyroblasts are inclusion-rich, while a few of them are inclusion-poor to inclusion-free. The inclusions are mostly quartz with minor amounts of biotite, muscovite, plagioclase, ilmenite, allanite, zircon and xenotime. Distinct inclusion trails with patterns ranging from curved to sinusoidal, sigmoidal and snowball can be seen in the garnet porphyroblasts. Inclusion trails in some of the porphyroblasts are continuous with the matrix foliation and indicate syntectonic growth of garnet during the shearing event. Petrography of individual samples from increasing structural level along the Alaknanda Valley is outlined below.

3.1.2. Sample M37: assemblage grt–chl–bt–ms–pl–qz–ilm–tur–aln

M37 is the structurally lowest garnet-bearing sample in the MCTZ and marks the garnet-in isograd in the field. Biotite–muscovite-rich layers with minor chlorite are intercalated with quartz–plagioclase-rich layers. Garnet occurs as anhedral porphyroblasts (~500–2000 µm size) with occasional inclusions of ilmenite (Figs.2a, b). Allanite and monazite occur as accessory phases in the matrix. A rare sphalerite grain of ~ 40 µm diameter is present in the matrix (Fig.2b).

3.1.3. Sample M19: assemblage grt–chl–bt–ms–pl–qz–ilm–tur–aln

Sample M19 is rich in felsic minerals compared to phyllosilicates. Modal abundance of plagioclase in the sample is high compared to that in M37. Garnet porphyroblasts (~750–1750 µm size) are anhedral in shape and commonly display spiral inclusion trails, which are continuous with the matrix foliation (Fig.2c). The inclusion trails are mostly of quartz and ilmenite with a few grains of biotite, muscovite, chlorite, plagioclase and allanite. Allanite forms small equant to elongate grains of ~20–25 µm length and occurs both as inclusions in the rim of garnet porphyroblasts and as a matrix phase (Fig.2d). Matrix allanite grains are commonly aligned parallel to the main foliation (S_e), while allanite inclusions in garnet porphyroblasts are aligned parallel to the inclusion trail pattern. Monazite occurs as amoeboid shaped grains of up to ~200 µm length in the matrix.

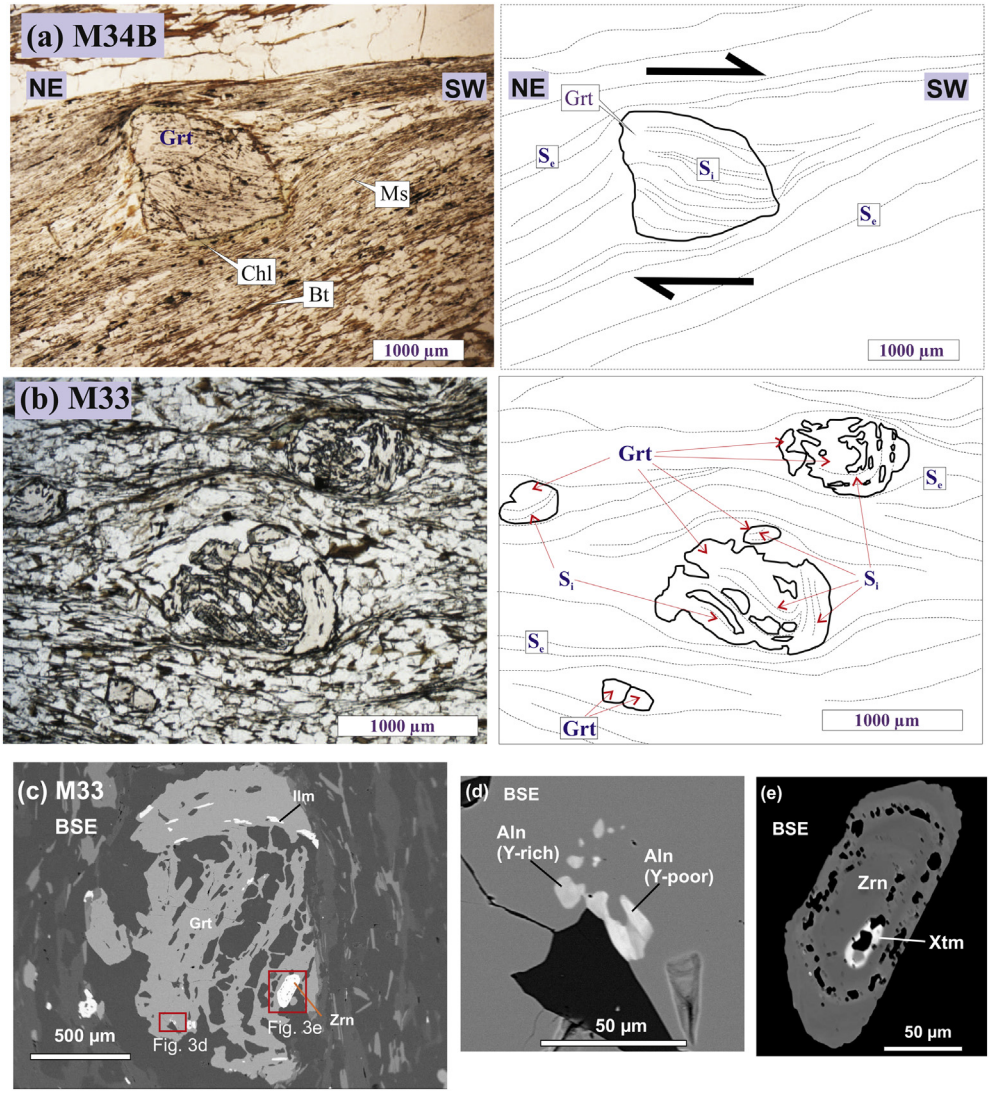

Fig.3. Photomicrographs and corresponding line drawings (a, b)and BSE images (c, d, e)of MCTZ samples. (a)Gently curved inclusion trails (S_i) in garnet porphyroblast continuous with the external foliation (S_e) (sample M34B; plane polarised light); (b)Photomicrograph with line drawing showing porphyroblast-matrix (S_i-S_e) relationship. Garnet porphyroblast with inclusion-rich core showing sinusoidal pattern (S_i) and inclusion-poor rim with gently curved S_i (sample M33; plane polarised light); (c)garnet porphyroblast with inclusions of allanite, ilmenite and zircon (sample M33); (d)enlarged view of allanite inclusion in sample M33. Note that the Y content of allanite is variable with brighter shade representing relatively Y-rich composition; (e)enlarged view of zircon inclusion in garnet from sample M33; the zircon inclusion contains xenotime inclusion within it.

3.1.4. Sample M34B: assemblage grt–chl–bt–ms–pl–qz–ilm–tur–aln

Quartz-rich felsic layers are intercalated with phyllosilicate layers. Plagioclase is rare, while the modal abundance of garnet is the highest among all the studied samples. Large anhedral porphyroblasts of garnet (~700–3600 µm size) commonly exhibit curved to helicitic inclusion trails of quartz, biotite, muscovite and ilmenite which are continuous with the matrix foliation (Fig.3a). Allanite occurs as inclusion in the garnet rim and also as discrete grains in the matrix. The allanite inclusions are commonly prismatic in shape and aligned parallel to the inclusion trail pattern within garnet. No monazite is detected in the sample.

3.1.5. Sample M33: assemblage grt–chl–bt–ms–pl–qz–ilm–tur–aln

This sample is from the structurally highest level in the MCTZ along the Alaknanda Valley. It is quartz-rich with a relatively small modal amount of plagioclase. Muscovite is much more abundant than biotite. The S_1 matrix foliation generally wraps around garnet porphyroblasts (Fig.3b). One of the porphyroblasts (~1620 µm size) displays sinusoidal inclusion trails that are continuous with the matrix foliation (Fig.3c). Quartz, biotite and ilmenite are the common inclusion phases in garnet, while equant to elongate inclusions of allanite of ~20–25 µm length are occasionally present in the garnet rim (Figs.3c, d). A zircon grain of ~180 µm length occurs as inclusion in the rim of the garnet porphyroblast and in turn contains inclusion of xenotime (Fig.3e). No monazite is detected in the rock.

3.2. HHCS rocks

3.2.1. General characteristics

HHCS rocks occurring immediately above the MCTZ are marked by the appearance of microscopic needles of kyanite (Fig.4a), whereas at higher structural levels somewhat larger kyanite grains can be observed (Fig.4b). No chlorite is present in the HHCS rocks. Unlike the garnet porphyroblasts from the MCTZ rocks, the HHCS garnets show random orientation of mineral inclusions (Figs.4c, d).

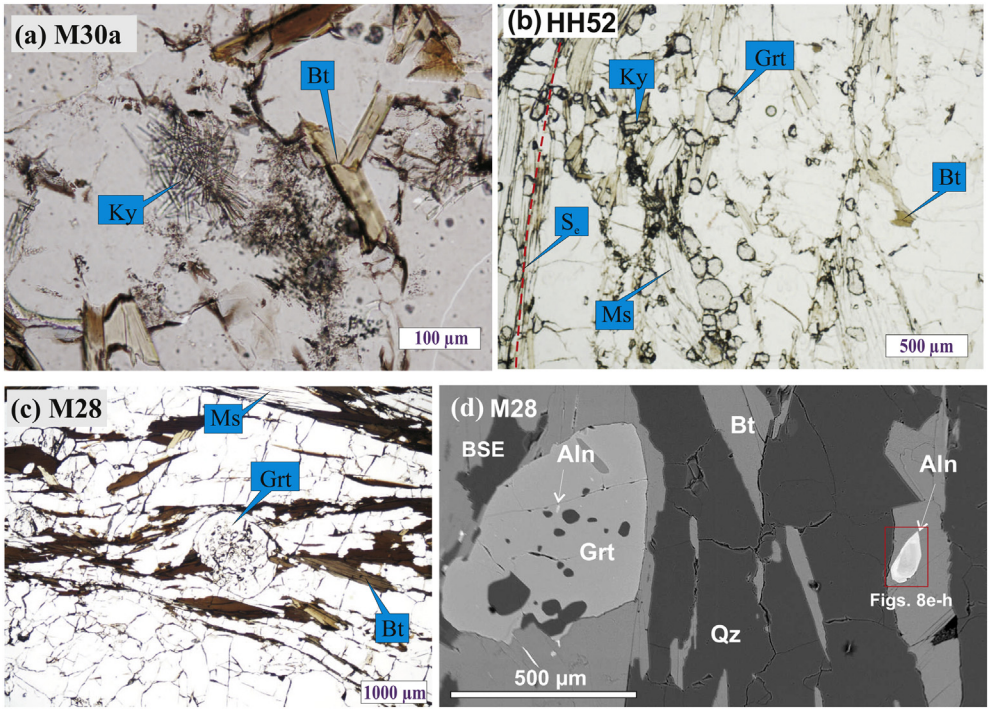

Fig.4. Photomicrographs (a–c) and a BSE image (d)of the HHCS samples. (a)Cluster of kyanite needles in sample M30a (plane polarised light); (b)Small kyanite blades and anhedral garnet grains in sample HH52 (plane polarised light); (c)Photomicrograph showing anhedral garnet porphyroblast with randomly oriented inclusion pattern in sample M28 (plane polarised light); (d)BSE image of a garnet porphyroblast in sample M28 containing randomly oriented inclusions of allanite and quartz. Note the large allanite grain in the matrix.

3.2.2. Sample M28: assemblage grt–ky–bt–ms–pl–qz–ilm–rt–aln

The sample contains a rare cluster of microscopic needles of kyanite and represents the structurally lowest level of the HHCS. It is rich in biotite relative to muscovite. Garnet occurs as anhedral porphyroblasts with a size range of ~725–1500 µm and contains randomly-oriented inclusions, which are mostly of quartz (Fig.4c) and occasionally of ilmenite, rutile, biotite, muscovite, apatite, plagioclase and allanite. Allanite inclusions can be found in the core as well as rim of garnet porphyroblasts and are randomly oriented. Allanite grains also occur in the matrix and are usually larger in size (up to ~150 µm long) (Fig.4d) than allanite inclusions in garnet. The sample is devoid of monazite.

3.2.3. Sample HH52: assemblage grt–ky–bt–ms–pl–qz–ilm

This sample is from a higher structural level than M28 and shows alternating bands of felsic and mafic minerals. Small kyanite blades are locally developed (Fig.4b). Garnet grains are anhedral in shape with a size range of ~100–500 µm and are mostly devoid of inclusions barring occasional randomly oriented grains of ilmenite. Relatively large monazite grains (~175–250 µm long) occur in the matrix of the rock.

4. Analytical methods

Back-scattered electron (BSE) imaging, elemental X-ray mapping, and quantitative analyses of garnet, allanite and monazite in polished thin sections were carried out using a five channel WDS CAMECA SX-fiveEPMA at IIT Bombay, Mumbai, India. Major elemental X-ray maps of garnet were generated at acceleration voltages of 15–20 kV and beam current of 100 nA. Elemental X-ray maps of garnet, monazite and allanite in selected samples were generated at acceleration voltages of 15–20 kV and beam current of 100 nA. Line scan analyses of garnet in two MCTZ samples (M19 and M34B) for the elements Si, Ti, Al, Fe, Mn, Mg, Ca, Na and Y were carried out at an acceleration voltage of 15 kV, beam current of 300 nA and nominal beam diameter of 1 µm. Major, minor and trace elements in allanite (Si, Ti, Al, Fe, Mn, Mg, Ca, Th, U, Y, La, Ce, Pr, Nd, Sm) and monazite (Si, Al, Ca, P, Th, U, Pb, Y, La, Ce, Pr, Nd, Sm, Gd, Dy) in five samples (M37, M19, M34B, M33, M28) were analysed at an acceleration voltage of 15 kV, beam currents of 100 nA (allanite) and 200 nA (monazite), and nominal beam diameter of 1 µm. Full calibration settings for garnet, allanite and monazite analyses are given in Supplementary TableA1. Matrix correction was done using the X-PHI method (Merlet, 1992). The detection limits are the lowest concentrations of the element present that is statistically above the background continuum level by 3 sigma and were determined with the Cameca software following the method of Ancey et al. (1978).

Quantitative point analyses of chlorite, biotite, muscovite, plagioclase and garnet rim in the MCTZ sample M33 and a quantitative line scan for major element analyses for one garnet porphyroblast in the HHCS sample M28 were carried out at the Wadia Institute of Himalayan Geology, Dehradun using the CAMECASX-100 at an acceleration voltage of 15 kV, beam current of 20 nA and beam diameter of 1 µm. Matrix correction was done by using the PAP method (Pouchon and Pichoir, 1984).

Major and trace element analyses for bulk rocks were carried out at the Wadia Institute of Himalayan Geology, Dehradun on pressed pellets using a SIEMENS SRS 3000 XRF instrument. The analytical precision is better than 5% for major oxides and 12% for trace elements. The standard deviation of repeated measurements is better than 2%.

5. Analytical results

The ranges of Y content in garnet, allanite and monazite are given in Table3. Representative analyses of garnet, allanite and monazite in different samples are presented in Tables4 to 6, respectively. A full set of allanite analyses is given in the Supplementary TableA2. EPMA analyses of biotite, chlorite, muscovite and plagioclase in sample M33 are given in Table7. YX-ray maps of six garnet porphyroblasts (one each from four MCTZ samples M37, M19, M34B, M33 and two from HHCS sample M28) are shown in Fig.5. X-ray elemental maps of Ca, Fe, Mg, Mn for four garnet porphyroblasts can be found in Thakur et al. (2015), while those for the remaining two (i.e. garnets from M33, M28) are shown in Figs.6 and 7. Y, Ce and Th X-ray maps of allanite grains from samples

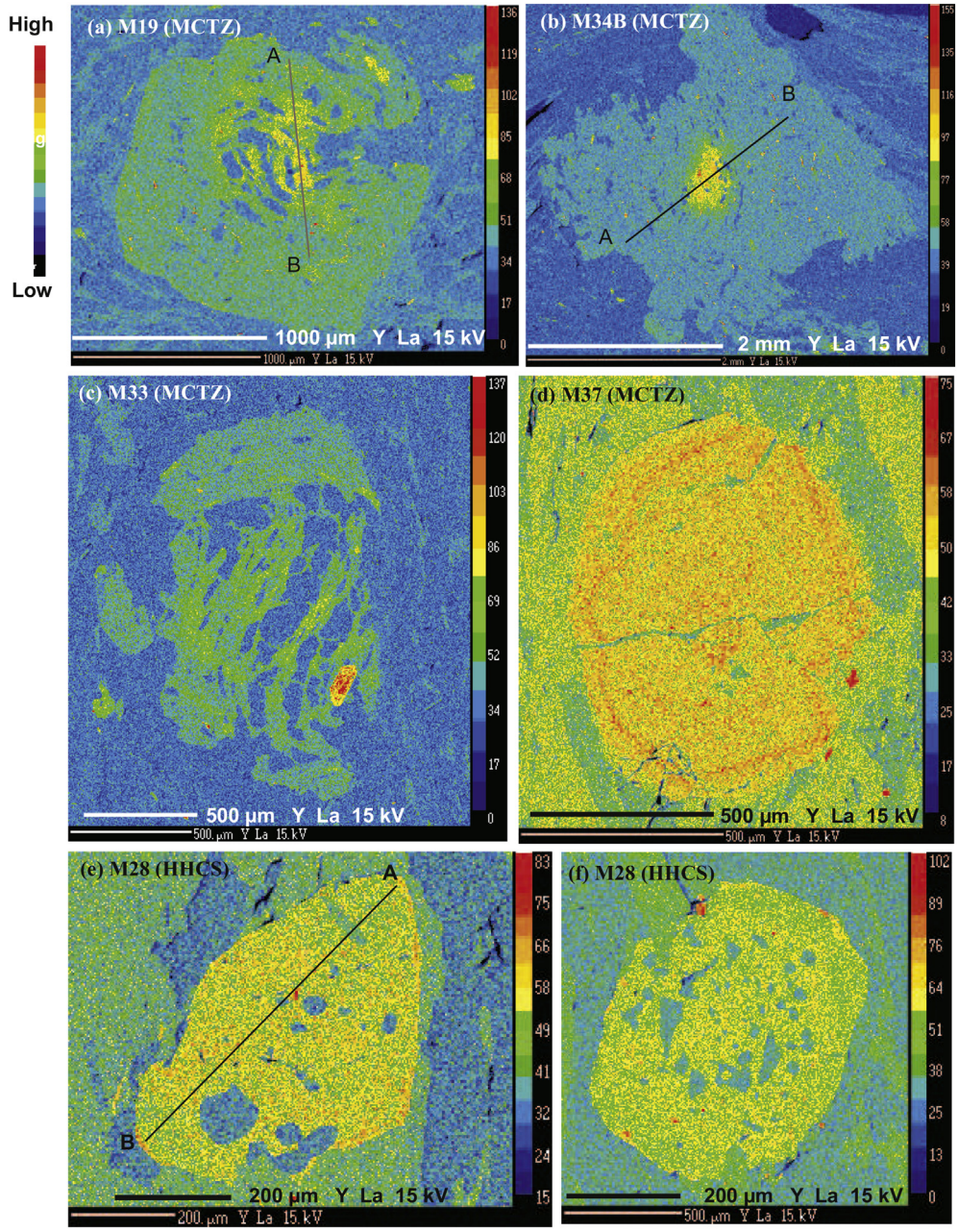

Fig.5. X-ray elemental maps of yttrium in garnet porphyroblasts from the MCTZ (a–d) and HHCS (e–f) samples. (a)garnet from sample M19 with Y-rich core with a spiral pattern and Y-poor rim; (b)narrow Y-rich core and wide Y-poor rim in garnet from sample M34b; (c)garnet from sample M33 showing weak Y zoning with higher Y in the core; (d)garnet from sample M37 showing a Y-rich annulus towards the rim; (e, f)garnet porphyroblasts from sample M28 with a slight increase in Y content at the rim (e). 'A–B' represents the line along which composition profile was taken.

M19 and M28, and YX-ray map of monazite grains from sample M19 and HHCS sample HH52 are presented in Fig.8.

5.1. Mineral chemistry

5.1.1. Garnet

Garnet porphyroblasts from the two MCTZ samples M19 and M34B show distinct chemical zoning with a high yttrium core (1733–3311 ppm) of variable width and Y-poor rim (< 143 ppm) (Table4; Figs.5a, b). Sample M19 shows asymmetrical Y zoning pattern with a broad low-Ydomain in the lower left and a high-Y domain in the centre-right part of the garnet porphyroblast (Fig.5a). Garnets from the MCTZ sample M33 show somewhat weak Y zoning with a wide core containing higher Y (811–1116 ppm) than the rim (Fig.5c). Overall, the general pattern of Y distribution in garnet porphyroblasts is a Y-rich core and Y-poor rim except for the MCTZ sample M37. A garnet from this sample shows a Y-rich annulus (up to ~398 ppm) near the rim, while Y content remains uniformly low in the rest of the porphyroblast (Fig.5d). Major element zoning maps for samples M19 and M34B show normal type of element distribution with smoothly decreasing X_{sps} and increasing X_{prp} from the core to the rim, while X_{alm} and X_{grs} either show minor fluctuations or remain nearly uniform (Figs.9a, b). X-ray elemental maps for a garnet porphyroblast in the MCTZ sample M33 show distinct chemical zoning with decreasing Ca and Mn and increasing Mg from the core to the rim (Fig.6). Fe concentration is broadly uniform throughout the grain.

In the HHCS sample M28, garnet shows broadly homogeneous composition except near biotite inclusions and at the outermost rim where

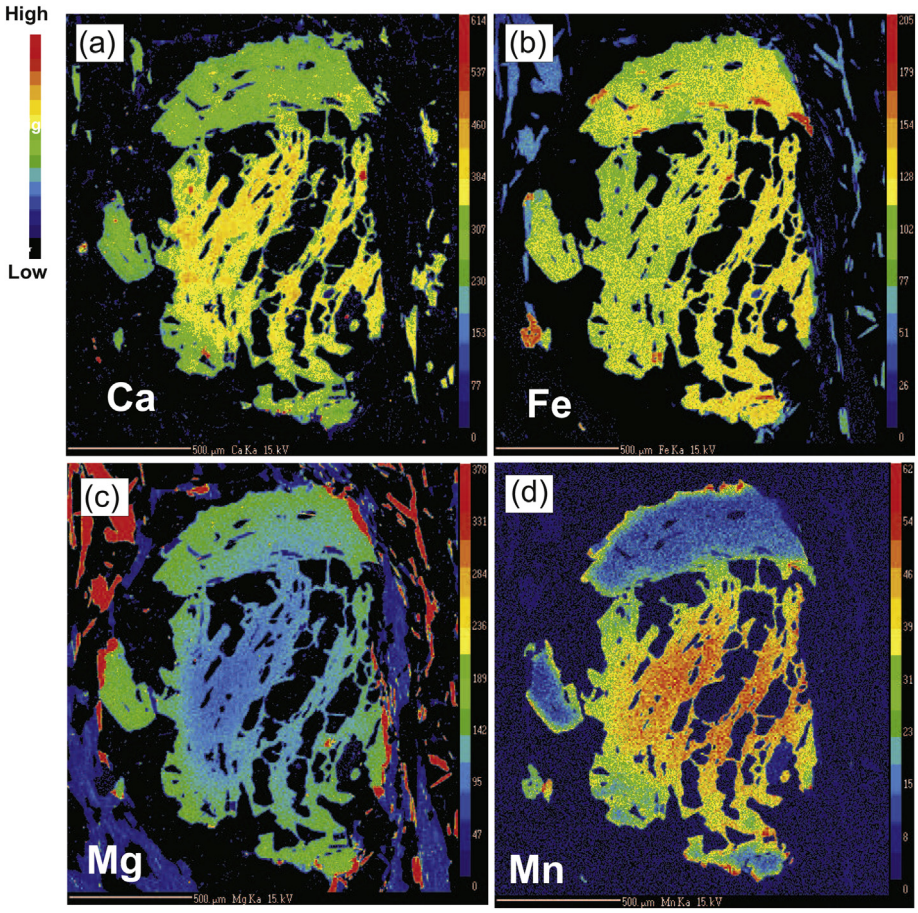

Fig.6. X-ray elemental maps of Ca (a), Fe (b), Mg (c)and Mn (d)of a garnet porphyroblast in MCTZ sample M33. The garnet porphyroblast shows chemical zoning with decreasing Ca and Mn and increasing Mg from core to rim. Fe content is broadly uniform throughout the crystal.

X_{sps} increases sharply that is balanced by a decrease in X_{prp}(Figs.7 and 9c). The Y content slightly increases at the garnet rim and Ti remains nearly uniform throughout the porphyroblast (Fig.9c).

5.1.2. Allanite

BSE images and elemental X-ray maps reveal that allanite grains are strongly zoned with respect to Y, Ce and Th in both MCTZ(Figs.8a–d) and HHCS(Figs.8e–h) rocks. The concentrations of these elements in allanite vary widely within individual samples and from one sample to the other. The Y_2O_3 contents are below detection limit (b.d.) to 3.45 wt% in sample M19 and b.d. to 0.29 wt% Y_2O_3 in sample M34B (Table5; Supplementary TableA2). Allanite inclusions in a garnet porphyroblast from sample M33 (Fig.3d) have highly variable Y_2O_3 (0.25–1.29 wt%), while allanite grains in the matrix of the rock have Y concentration below detection limit. Allanite in the HHCS sample M28 contains b.d.–0.77 wt% Y_2O_3.

$\Sigma LREE_2O_3$ content of allanite falls in a wide range of 6.61–21.55 wt%. The concentrations of different LREEs are: La_2O_3 (1.51–5.65 wt%), Ce_2O_3 (3.01–10.25 wt%), Nd_2O_3 (1.35–4.03 wt%), Pr_2O_3 (0.35–1.17 wt%) and Sm_2O_3 (0.23–0.89 wt%). La/Nd ratios of the mineral fall between 0.99 and 1.57. Chondrite-normalisedLREE patterns of allanite show a gradual depletion from La to Sm in all the samples (Fig.10). In most samples, allanite grains in the matrix are enriched in LREEs relative to allanite inclusions in garnet, although the magnitude of enrichment shows variation (Fig.10). The differences in the average $\Sigma LREE_2O_3$ content of matrix allanite grains and allanite inclusions in garnet are 8.08 wt% and 1.43 wt % in the MCTZ samples in M19 and M33, respectively and 2.24 wt% in the HHCS sample M28 (Supplementary TableA3). In the MCTZ sample M34B, matrix allanites are slightly poorer in average $\Sigma LREE_2O_3$ than allanite inclusions in garnet with a difference of 0.79 wt%. An allanite grain from M28 clearly shows oscillatory zoning in Ce, Th and Y

Table3
Yttrium content of minerals in MCTZ and HHCS rocks. b.d. = below detection limit. "–" = absent.

	Mode of occurrence	MCTZ samples				HHCS samples	
		M37	M19	M34B	M33	M28	HH52
Garnet	Porphyroblast	b.d.–398 ppm	b.d.–2444 ppm	b.d.–3311 ppm	b.d.–1116 ppm	b.d.–562 ppm	Not analysed
Allanite	Inclusion in garnet porphyroblast	–	1.83–3.45 wt%	0.15–0.22 wt%	0.25–1.29 wt%	0.31–0.36 wt%	–
	Grains in the matrix	b.d.	b.d.–1.01 wt%	b.d.–0.29 wt%	b.d.	b.d.–0.77 wt%	–
Monazite	Inherited grains in the matrix	0.44–0.60 wt%	1.08–1.58 wt%	–	–	–	0.04–1.62 wt%
Xenotime	Within zircon inclusion in garnet porphyroblast	–	–	–	Nearly pure YPO_4 phase	–	–

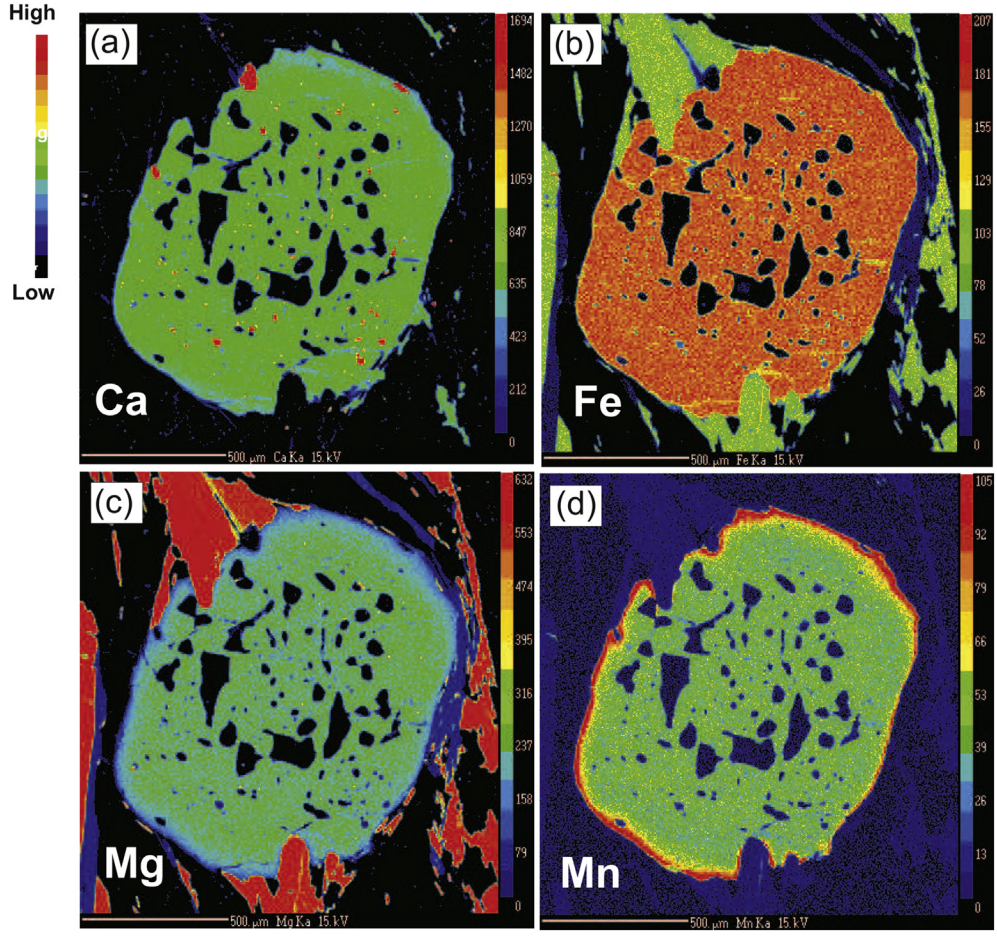

Fig.7. X-ray elemental maps of Ca (a), Fe (b), Mg (c), and Mn (d)of a garnet porphyroblast in HHCS sample M28. The porphyroblast is broadly homogeneous in composition except for a thin Mn-rich rim.

(Figs.8f–h) with considerable fluctuations in Ce, La, Nd and Y(Fig.11a) and a negative correlation between Al and ΣLREE (Fig.11b).

5.1.3. Monazite

Monazite occurs in the matrix of the MCTZ samples M19 and M37, and the HHCS sample HH52. Their $LREE_2O_3$ contents fall in the range of 57.34–63.44 wt% that includes fairly high values of Ce_2O_3 (24.57–29.38 wt%), La_2O_3 (12.35–16.05 wt%) and Nd_2O_3 (10.51–13.10 wt%) and low values of Pr_2O_3 (2.70–3.23 wt%), Sm_2O_3 (1.98–3.25 wt%), Gd_2O_3 (0.85–2.29 wt%) and Dy_2O_3 (b.d.–0.63 wt%) (Table6). The Y_2O_3 content of monazite varies from one sample to the other i.e. 1.08–1.58 wt% in sample M19, 0.44–0.60 wt% in M37, and 0.04–1.62 wt% in HH52. However, La/Nd ratios of the monazites fall in a range of 1.02–1.49.

5.1.4. Other minerals

Biotite and chlorite from the MCTZ sample M33 have X_{Mg} values of ~0.46 and ~0.48, respectively, while plagioclase is sodic in nature with X_{ab} [= Na/(Na + Ca + K)] of ~0.84 (Table7). In this sample, the xenotime grain occurring within zircon inclusion in garnet has Y_2O_3 content of 41.22 wt%.

5.2. Bulk rock composition

Bulk rock analyses show that the studied samples have relatively high Al_2O_3 (17.74–23.21 wt%) and low CaO (0.49–1.68 wt%) contents compared to those of the average pelite (16.57 wt% Al_2O_3; 2.17 wt% CaO) (Shaw, 1956) (Table8). The Y content of the rocks falls in a narrow range of 26–30 ppm.

6. Phase diagram modelling and evolution of mineral assemblages

Phase diagrams for all the samples except M33 can be found in Thakur et al. (2015), the results from which are summarised in Table1. In the present study, a phase diagram was constructed for M33 using a fixed bulk rock composition (Fig.12). The phase diagram was calculated in the model chemical system MnNCKFMASHT using the PERPLEX_6.6.6 software package (Connolly, 2005; http://www.perplex.ethz.ch) considering an internally consistent thermodynamic dataset 'hp02ver.dat' (Connolly and Kerrick, 2002; Holland and Powell, 2003). Quartz was considered as an excess phase. A correction in CaO to the bulk rock composition was made assuming the presence of P_2O_5 only in apatite. H_2O was taken as an excess component and the amount considered was just enough to saturate the solidus. No ferric iron was considered for the phase diagram modelling, because: (1)presence of ilmenite and absence of magnetite/haematite in the samples indicate low oxidation condition (Diener and Powell, 2010; Groppo et al., 2009); (2)presence of sulphide mineral in the MCTZ sample M37 indicates reducing environment; and (3)stoichiometry indicates negligible ferric iron content in the silicate minerals. The mineral solution models used are Gt (HP), St (HP), hCrd for garnet, staurolite and cordierite, respectively (Holland and Powell, 1998), Chl (HP) for chlorite (Holland et al., 1998), San for sanidine (Thompson and Hovis, 1979), and melt (HP) for melt (White et al., 2001). Biotite in the MCTZ sample M33 is

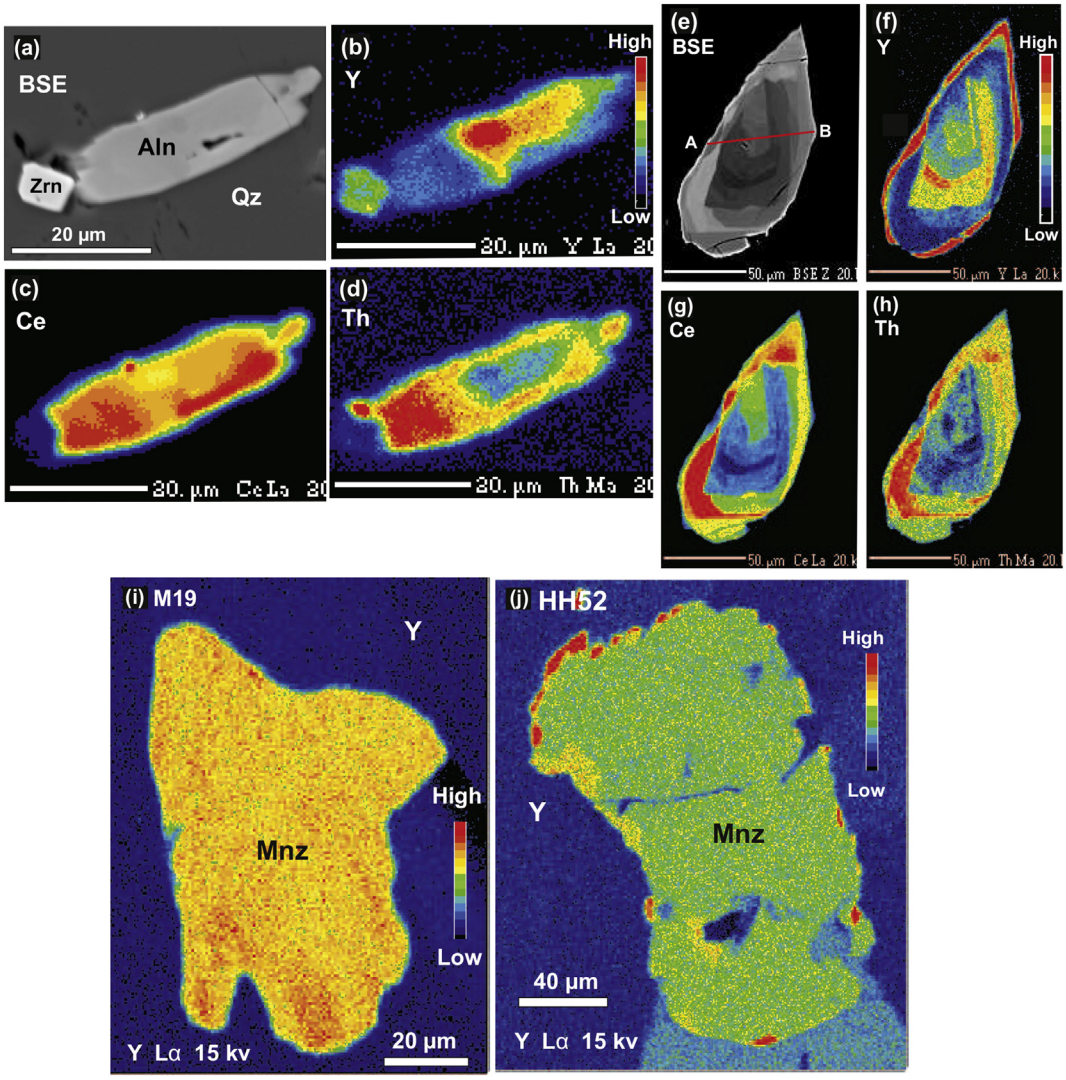

Fig.8. BSE image and X-ray elemental maps of Y, Ce and Th, respectively of allanite in MCTZ sample M19 (a–d) and HHCS sample M28 (e–h). Y X-ray map of monazite in MCTZ sample M19 (i)and HHCS sample HH52 (j).

titanium-bearing therefore the solution model TiBio (HP) (Powell and Holland, 1999) is used for this mineral. Similarly, the solution model AbPl (Newton et al., 1980) is chosen for plagioclase since it is albite-rich and contains negligible amount of orthoclase component in M33. For muscovite and paragonite occurring in MCTZ rocks, Mu and Pa solution models (Chatterjee and Froese, 1975), respectively were used.

The phase diagram shows that the assemblage chl–bt–ms–pl–qz ± spn ± ilm ± rt. is stable in a low *P–T* field (i.e. < 500 °C; < 7 kbar) (Fig.12a). With increasing grade of metamorphism garnet appears in the rock with a resulting assemblage of grt–bt–pg–mu–pl–qz–ilm. This assemblage is stable in the *P–T* ranges of ~500–585 °C and ~5.3–7.3 kbar. The *P–T* boundary representing the first appearance of garnet is shown in Fig.12b. Further increase in temperature results in the appearance of staurolite at a temperature of ~585 °C (at 7 kbar) (Fig.12b). Since staurolite is absent in the sample M33, the *P–T* boundary for the appearance of staurolite marks the upper limit of metamorphism for this rock. Melt bearing assemblages appear towards higher temperature side (> 680 °C) of the phase diagram. Plagioclase-bearing assemblages are stable at pressures <7 kbar (Fig.12b).

Compositional isopleths of X_{prp}, X_{sps} and X_{grs} of garnet core composition plotted in the phase diagram intersect at a point which yields *P–T* conditions of 570 °C and 6.5 kbar (Fig.12c). The *P–T* condition yielded by garnet core composition is higher than the temperature of the garnet-in line in Fig.12b which indicates overstepping of the garnet isograd reaction (Pattison et al., 2011; Spear et al., 2014). With increasing *P* and *T* the successive newly formed rim of the growing garnet changes its composition in accordance to the changing garnet isopleth values in the equilibrium phase diagram for fixed bulk-rock composition. Once garnet rim is incorporated within the growing garnet it no longer remains in equilibrium with the matrix phases and resultantly gives rise to zoned garnet. It is observed that compositional isopleths of X_{prp}, X_{sps} and X_{grs} for the garnet rim composition are sub-parallel to one another. Therefore, the *P–T* conditions of garnet rim is determined by using isopleths of X_{prp} in garnet, X_{Mg} in biotite and modal abundance of plagioclase. The intersection of these isopleths yield *P–T* values of 580 °C and 6.6 kbar (Fig.12d). Comparison of the *P–T* conditions for the core and rim compositions of garnet indicate prograde growth of the mineral (Fig.12e). The *P–T* path drawn for sample M33 is similar to that reported

Table4
Representative microprobe analyses of garnet. Cations are based on 12 oxygens.

	MCTZ sample							HHCS sample	
	M37	M19		M34B		M33		M28	
	core	core	rim	core	rim	core	rim*	core	rim
SiO_2	36.81	36.74	36.97	36.43	37.01	36.56	36.51	37.44	37.29
TiO_2	0.05	0.07	0.09	0.10	0.08	0.07	0.05	b.d.	0.02
Al_2O_3	20.60	20.49	20.69	20.28	20.55	20.65	20.64	20.91	20.82
FeO	33.58	31.38	32.14	33.46	34.00	33.74	34.56	30.12	30.55
MnO	2.42	2.59	1.17	2.50	1.41	2.24	1.00	1.28	1.39
MgO	1.67	1.86	2.08	1.48	2.23	2.02	2.49	3.79	3.49
CaO	4.18	4.90	5.47	3.53	3.43	3.94	3.46	5.65	5.48
Na_2O	0.05	0.07	b.d.	0.07	0.02	0.04	0.02	0.03	b.d.
Y (ppm)	398	2444	143	3311	b.d.	1116	n.a.	562	435
Total	99.41	98.41	98.62	98.27	98.73	99.40	98.73	99.29	99.10
Si	2.994	3.009	3.010	3.009	3.022	2.970	2.978	2.991	2.993
Ti	0.003	0.004	0.006	0.006	0.005	0.004	0.003	0.000	0.001
Al	1.975	1.978	1.985	1.974	1.978	1.977	1.984	1.969	1.970
Fe^{3+}	0.037	0.000	0.000	0.000	0.000	0.074	0.057	0.051	0.039
Fe^{2+}	2.247	2.149	2.188	2.311	2.322	2.219	2.300	1.962	2.012
Mn	0.167	0.179	0.081	0.175	0.097	0.154	0.069	0.087	0.095
Mg	0.203	0.226	0.252	0.182	0.272	0.245	0.303	0.451	0.417
Ca	0.365	0.430	0.478	0.313	0.300	0.343	0.302	0.484	0.471
Na	0.008	0.011	0.000	0.012	0.004	0.007	0.003	0.004	0.000
Y	0.002	0.014	0.001	0.018	0.000	0.006	n.a.	0.003	0.002
Total	8.000	8.000	8.000	8.000	8.000	8.000	8.000	8.000	8.000
X_{Mg}	0.08	0.10	0.10	0.07	0.10	0.10	0.12	0.19	0.17
X_{alm}	0.75	0.72	0.73	0.78	0.78	0.75	0.77	0.66	0.67
X_{prp}	0.07	0.08	0.08	0.06	0.09	0.08	0.10	0.15	0.14
X_{grs}	0.12	0.14	0.16	0.10	0.10	0.12	0.10	0.16	0.16
X_{sps}	0.06	0.06	0.03	0.06	0.03	0.05	0.02	0.03	0.03

b.d. = below the detection limit; n.a. = not analysed.
Detection limit (in ppm): *Si* = 116, *Ti* = 168, *Al* = 95, *Fe* = 355, *Mn* = 172, *Mg* = 73, *Ca* = 112, *Na* = 197, *Y* = 47.
* Analysed at accelartion voltage of 15 kV, beam current of 20 nA and beam diameter of 1 μm.

Table5
Representative microprobe analyses of allanite. Cations are based on 12.5 oxygens.

	MCTZ sample							HHCS sample	
	M37	M19		M34B		M33		M28	
	Matrix grain	Incl. in grt	Matrix grain	Incl. in grt	Matrix grain	Incl. in grt	Matrix grain	Incl. in grt	Matrix grain
SiO_2	34.36	34.81	34.24	32.33	32.39	33.12	33.43	35.18	35.03
TiO_2	0.06	0.06	0.07	0.03	0.07	0.09	0.10	0.11	0.10
ThO_2	1.80	0.10	0.62	0.14	1.81	1.51	2.29	0.42	0.65
UO_2	0.33	0.10	0.25	b.d.	b.d.	0.38	0.16	0.11	0.18
Al_2O_3	21.43	22.62	20.42	19.33	19.17	19.77	20.69	23.04	22.80
Y_2O_3	b.d.	3.45	1.01	0.22	0.29	1.29	b.d.	0.36	0.66
La_2O_3	3.87	1.51	3.58	5.22	4.44	2.94	4.31	2.12	2.34
Ce_2O_3	7.23	3.01	6.80	9.87	8.79	5.73	8.33	4.20	4.71
Pr_2O_3	0.82	0.46	0.84	1.17	1.08	0.72	1.00	0.48	0.62
Nd_2O_3	2.97	1.35	2.95	4.03	3.78	2.39	3.38	1.72	2.26
Sm_2O_3	0.57	0.28	0.57	0.74	0.71	0.49	0.58	0.37	0.54
FeO	9.70	10.65	11.11	12.05	11.46	12.22	10.22	9.76	7.83
MnO	0.08	0.40	0.23	0.12	0.15	0.64	0.38	0.03	0.03
MgO	0.34	0.15	0.26	0.19	0.16	0.54	0.65	0.52	0.45
CaO	13.72	16.17	13.21	11.86	11.53	13.95	11.87	16.59	16.87
Total	97.24	95.13	96.15	97.31	95.82	95.76	97.38	95.01	95.06
ΣLREE	15.45	6.61	14.73	21.03	18.80	12.25	17.60	8.89	10.47
Si	3.079	3.051	3.105	3.021	3.059	3.038	3.053	3.068	3.075
Ti	0.004	0.004	0.005	0.002	0.005	0.006	0.007	0.007	0.007
Th	0.037	0.002	0.013	0.003	0.039	0.032	0.048	0.008	0.013
U	0.007	0.002	0.005	0.000	0.000	0.008	0.003	0.002	0.003
Al	2.263	2.336	2.183	2.129	2.134	2.137	2.227	2.368	2.359
Y	0.000	0.142	0.043	0.010	0.013	0.056	0.000	0.015	0.027
La	0.128	0.049	0.120	0.180	0.155	0.099	0.145	0.068	0.076
Ce	0.237	0.097	0.226	0.338	0.304	0.192	0.278	0.134	0.151
Pr	0.027	0.015	0.028	0.040	0.037	0.024	0.033	0.015	0.020
Nd	0.095	0.042	0.096	0.135	0.128	0.078	0.110	0.053	0.071
Sm	0.017	0.009	0.018	0.024	0.023	0.015	0.018	0.011	0.016
Fe	0.727	0.780	0.843	0.942	0.905	0.937	0.780	0.711	0.575
Mn	0.006	0.030	0.018	0.009	0.012	0.050	0.029	0.002	0.002
Mg	0.045	0.019	0.035	0.026	0.022	0.074	0.089	0.068	0.059
Ca	1.317	1.519	1.283	1.187	1.167	1.370	1.161	1.550	1.587
Total	7.990	8.097	8.017	8.046	8.001	8.116	7.983	8.082	8.042
X_{Mg}	0.06	0.02	0.04	0.03	0.02	0.07	0.10	0.09	0.09
La/Nd	1.35	1.16	1.25	1.34	1.21	1.27	1.32	1.28	1.07

Detection limit (in ppm): *Si* = 178, *Ti* = 130, *Th* = 237, *U* = 254, *Al* = 176, *Y* = 138, *La* = 265, *Ce* = 283, *Pr* = 829, *Nd* = 873, *Sm* = 642, *Fe* = 514, *Mn* = 180, *Mg* = 119, *Ca* = 228.

for other MCTZ and HHCS samples from the area (Thakur et al., 2015) (Fig.12e).

7. Discussion

7.1. Stability of allanite

Allanite occurs in rocks from garnet grade to kyanite grade in the study area. Many workers have proposed that the breakdown of allanite gives rise to monazite at the staurolite-in isograd during prograde metamorphism (Gasser et al., 2012; Goswami-Banerjee and Robyr, 2015; Janots et al., 2006, 2008; Rasmussen et al., 2006; Smith and Barreiro, 1990; Tomkins and Pattison, 2007; Yang and Pattison, 2006). However, in the Alaknanda Valley, the presence of allanite and absence of monazite in the kyanite grade HHCS sample M28 suggest that allanite is a stable metamorphic phase up to kyanite grade. Occurrence of allanite in kyanite grade rocks has been reported from a few areas (Finger et al., 2016; Janots et al., 2008; Wing et al., 2003) where its stabilisation can be attributed to the bulk compositional effect (Budzyn et al., 2017; Spear, 2010). For an average pelite with 16.57 wt% Al_2O_3 and 2.17 wt% CaO, Spear (2010) thermodynamically demonstrated that the allanite–monazite transition occurs at ~550 °C at a pressure of ~12 kbar and that with decreasing CaO and increasing Al_2O_3 contents the transition moves towards lower temperature. However, Wing et al. (2003) showed that in natural pelitic sequences allanite is stabilised to higher temperatures by increasing whole-rock Al_2O_3 content. We infer that the high-Al_2O_3 content in sample M28 (i.e. ~18.66 wt%, Table8) relative to the average pelite in Spear (2010) has expanded the stability field of allanite towards higher temperature. Although the CaO content of M28 (0.84 wt%, Table8) is lower than that of the average pelite, its effect on shifting the allanite–monazite transition towards lower temperature (Budzyn et al., 2017; Spear, 2010) has been overwhelmed by the effect of increased alumina content of the rock. Consequently, the rock has remained inside the allanite stability window. In addition to this, overstepping of allanite-monazite transition may have further influence the stability of allanite towards high temperature (Pattison et al., 2011; Spear et al., 2014).

7.2. Change in allanite chemistry with increasing structural level in the MCTZ

Distinct changes in allanite chemistry is observed with increasing structural level of rocks from the Alaknanda section. ΣLREE in allanite first increases from the lower structural level to the middle structural level and then decreases towards the upper structural level in the MCTZ which continues to the basal part of the HHCS. This is complemented by variation in the Al content of the mineral (Fig.13) which indicates the coupled substitution $REE^{3+} + Fe^{2+} = Al^{3+} + Ca^{2+}$ (Deer et al., 1986). The compositional variation of allanite appears to be linked with the modal abundance of garnet in the rocks from different structural levels. The garnet modal abundance increases significantly from the lower structural level to the middle structural level, reaches a maximum in sample M34B in the MCTZ, and then decreases further upsection (Table2) across the MCT (i.e. Vaikrita thrust). The

Table6
Representative microprobe analyses of monazite. Cations are based on 4 oxygens.

	M37 (MCTZ sample)					M19 (MCTZ sample)						HH52 (HHCS sample)					
	Grain 1	Grain 2		Grain 3		Grain 1	Grain 2		Grain 3			Grain 1	Grain 2		Grain 3		
Point no.	1/1	1/2	2/1	2/2	3/1	1/1	1/2	2/1	2/2	3/1	3/2	1/1	1/2	2/1	2/2	3/1	3/2
SiO_2	0.35	0.34	0.29	0.28	0.35	0.44	0.53	0.40	0.26	0.32	0.45	0.53	0.48	0.47	0.46	0.39	0.46
ThO_2	4.34	4.34	3.34	3.07	3.74	5.23	7.14	5.94	3.15	4.17	5.22	6.54	6.62	6.43	5.55	4.34	4.94
UO_2	b.d.	0.47	0.35	0.38	0.41	0.41	0.63	0.68	0.41	0.34	0.53	1.32	1.45	0.39	1.08	1.43	1.15
PbO	0.02	b.d.	b.d.	b.d.	b.d.	0.06	0.08	0.06	0.04	0.05	0.05	0.08	0.08	0.07	0.07	0.06	0.06
Al_2O_3	0.02	b.d.	0.02	b.d.	b.d.	b.d.	b.d.	b.d.	b.d.	b.d.	0.02	b.d.	b.d.	b.d.	b.d.	b.d.	b.d.
Y_2O_3	0.51	0.60	0.44	0.49	0.55	1.21	1.49	1.58	1.08	1.22	1.35	0.06	0.11	1.62	0.05	0.04	0.35
La_2O_3	15.24	15.36	15.73	15.67	15.67	15.09	13.40	14.10	15.26	15.96	14.28	14.32	14.09	12.35	14.54	16.05	13.10
Ce_2O_3	28.79	28.49	29.15	29.38	28.79	26.46	25.69	25.80	28.28	26.80	27.01	27.63	27.12	24.57	28.05	29.28	27.08
Pr_2O_3	3.14	3.17	3.23	3.23	3.20	2.85	2.79	2.70	2.93	2.85	2.91	2.95	2.89	2.80	2.97	2.98	3.16
Nd_2O_3	11.44	11.27	11.44	11.60	10.95	11.37	10.98	10.51	11.17	11.62	11.14	11.11	11.20	12.45	11.51	11.09	13.10
Sm_2O_3	2.10	2.06	2.05	2.17	1.98	2.44	2.44	2.31	2.34	2.46	2.43	2.29	2.35	3.25	2.29	2.18	2.91
Gd_2O_3	1.30	1.27	1.16	1.19	1.16	1.66	1.54	1.39	1.31	1.62	1.45	1.02	1.09	2.29	1.05	0.85	1.57
Dy_2O_3	0.29	0.24	0.20	0.20	0.20	0.45	0.57	0.53	0.41	0.47	0.47	0.06	0.07	0.63	0.05	b.d.	0.16
CaO	0.77	0.85	0.65	0.63	0.79	0.97	1.39	1.19	0.69	0.85	1.03	1.37	1.42	1.24	1.22	1.02	1.06
P_2O_5	30.65	30.52	30.72	30.75	31.17	30.13	30.01	30.45	30.71	30.22	30.26	30.43	30.23	30.93	29.82	30.41	30.04
Total	98.94	98.99	98.76	99.03	98.96	98.75	98.67	97.62	98.04	98.95	98.58	99.71	99.19	99.49	98.71	100.10	99.12
ΣLREE	62.28	61.86	62.96	63.44	61.95	60.30	57.39	57.34	61.70	61.77	59.68	59.38	58.81	58.34	60.46	62.42	61.08
Si	0.037	0.037	0.031	0.030	0.038	0.047	0.057	0.044	0.029	0.034	0.048	0.057	0.052	0.050	0.050	0.041	0.049
Th	0.107	0.107	0.082	0.075	0.092	0.128	0.176	0.149	0.078	0.102	0.128	0.161	0.164	0.158	0.137	0.105	0.121
U	0.000	0.011	0.008	0.009	0.010	0.010	0.015	0.017	0.010	0.008	0.013	0.032	0.035	0.009	0.026	0.034	0.027
Pb	0.001	0.000	0.000	0.000	0.000	0.002	0.002	0.002	0.001	0.001	0.001	0.002	0.002	0.002	0.002	0.002	0.002
Al	0.003	0.000	0.002	0.000	0.000	0.000	0.000	0.000	0.000	0.000	0.003	0.000	0.000	0.000	0.000	0.000	0.000
Y	0.029	0.035	0.025	0.028	0.032	0.069	0.086	0.093	0.063	0.070	0.077	0.004	0.006	0.093	0.003	0.002	0.020
La	0.607	0.611	0.628	0.623	0.628	0.598	0.534	0.573	0.615	0.631	0.567	0.570	0.565	0.492	0.581	0.631	0.520
Ce	1.137	1.125	1.155	1.159	1.145	1.040	1.016	1.041	1.131	1.052	1.065	1.092	1.080	0.973	1.112	1.143	1.066
Pr	0.123	0.124	0.128	0.127	0.127	0.111	0.110	0.108	0.117	0.111	0.114	0.116	0.114	0.110	0.117	0.116	0.124
Nd	0.441	0.434	0.442	0.447	0.425	0.436	0.424	0.414	0.436	0.445	0.428	0.428	0.435	0.481	0.445	0.422	0.503
Sm	0.078	0.076	0.077	0.080	0.074	0.090	0.091	0.088	0.088	0.091	0.090	0.085	0.088	0.121	0.085	0.080	0.108
Gd	0.046	0.046	0.042	0.043	0.042	0.059	0.055	0.051	0.047	0.058	0.052	0.037	0.039	0.082	0.038	0.030	0.056
Dy	0.010	0.008	0.007	0.007	0.007	0.015	0.020	0.019	0.014	0.016	0.016	0.002	0.002	0.022	0.002	0.000	0.006
Ca	0.089	0.098	0.075	0.073	0.092	0.111	0.161	0.141	0.080	0.098	0.119	0.158	0.165	0.144	0.142	0.116	0.122
P	2.800	2.787	2.815	2.806	2.867	2.740	2.745	2.841	2.840	2.743	2.760	2.780	2.783	2.832	2.734	2.746	2.735
Total	5.508	5.500	5.516	5.507	5.579	5.457	5.491	5.580	5.548	5.460	5.483	5.522	5.532	5.570	5.472	5.469	5.458
La/Nd	1.38	1.41	1.42	1.39	1.48	1.37	1.26	1.39	1.41	1.42	1.32	1.33	1.30	1.02	1.30	1.49	1.03

Detection limit (in ppm): *Si* = 129, *Th* = 114, *U* = 128, *Pb* = 118, *Al* = 125, *Y* = 253, *La* = 308, *Ce* = 326, *Pr* = 646, *Nd* = 684, *Sm* = 514, *Gd* = 835, *Dy* = 500, *Ca* = 157, *P* = 319.

Table7
EPMA analyses of chlorite, biotite, muscovite and plagioclase in MCTZ sample M33.

	bt	chl	pl	ms
SiO_2	35.88	23.12	63.84	46.48
TiO_2	1.49	0.06	0.02	0.42
Al_2O_3	18.04	20.90	21.49	34.83
FeO	19.82	25.49	0.23	1.16
MnO	0.18	0.11	b.d.	b.d.
MgO	9.54	13.45	b.d.	0.79
CaO	0.08	0.01	3.43	0.03
Na_2O	0.21	b.d.	10.29	1.55
K_2O	9.49	0.02	0.09	9.27
Total	94.73	83.16	99.39	94.53
Oxygen basis	22	28	8	22
Si	5.513	5.183	2.843	6.200
Ti	0.172	0.010	0.001	0.042
Al	3.267	5.522	1.128	5.476
Fe	2.547	4.778	0.009	0.129
Mn	0.023	0.021	0.000	0.000
Mg	2.185	4.494	0.000	0.157
Ca	0.013	0.002	0.164	0.004
Na	0.063	0.000	0.888	0.401
K	1.860	0.006	0.005	1.577
Total	15.643	20.047	5.040	14.009
X_{Mg}	0.46	0.48		0.55
X_{ab}			0.84	
X_{an}			0.15	
X_{or}			0.00	

Detection limit is <0.01 wt% (except FeO, b.d. <0.02).
X_{Mg} = Mg/(Mg + Fe); X_{ab} = Na/(Na + Ca + K); X_{an} = Ca/(Na + Ca + K); X_{or} = K/(Na + Ca + K).

amount and composition of garnet are dictated by bulk-rock composition which in turn affect the accessory phases. Since garnet is a major Al-bearing phase and prefers HREE to LREE in its crystal structure (e.g. Otamendi et al., 2002; Shrestha et al., 2017), high modal abundance of the mineral in M34B possibly resulted in the reduced availability of Al and increased supply of ΣLREE for allanite growth.

7.3. Origin of Y zoning in garnet

Garnet-bearing assemblage in the Alaknanda Valley has developed from a chl–bt-bearing assemblage which is evidenced by the presence of chlorite, biotite and muscovite as inclusions in garnet porphyroblasts. The phase diagram modelling shows that garnet starts to appear from this assemblage along an assumed Barrovian *P–T* path at ~500 °C and < 5 kbar pressure. The most likely garnet-forming reaction is:

Chlorite + muscovite + quartz = garnet + biotite + H_2O.

Garnet porphyroblasts from the MCTZ rocks not only show strong chemical zoning of Y but also zoning of major elements. Decreasing X_{sps} and increasing X_{Mg} and X_{prp} from the core to the rim (Figs.9a, b)is typical of garnets growing during prograde metamorphism (Caddick et al., 2010; Hollister, 1966 and references therein). The formation of Y-rich core and Y-poor rim (Figs.5a–c) along with the major element zoning suggests that the Y zoning has developed during prograde metamorphism. However, the Y zoning pattern does not quite match with the geometry of major element zoning because the Y enrichment has occurred in a relatively narrow core, while major element variations define a broader core (Figs.9a, b). Such Y zoning is possibly the result of partitioning with a Y-bearing accessory phase during the growth of the garnet rim (e.g. Mottram et al., 2015; Wang et al., 2015). Garnet

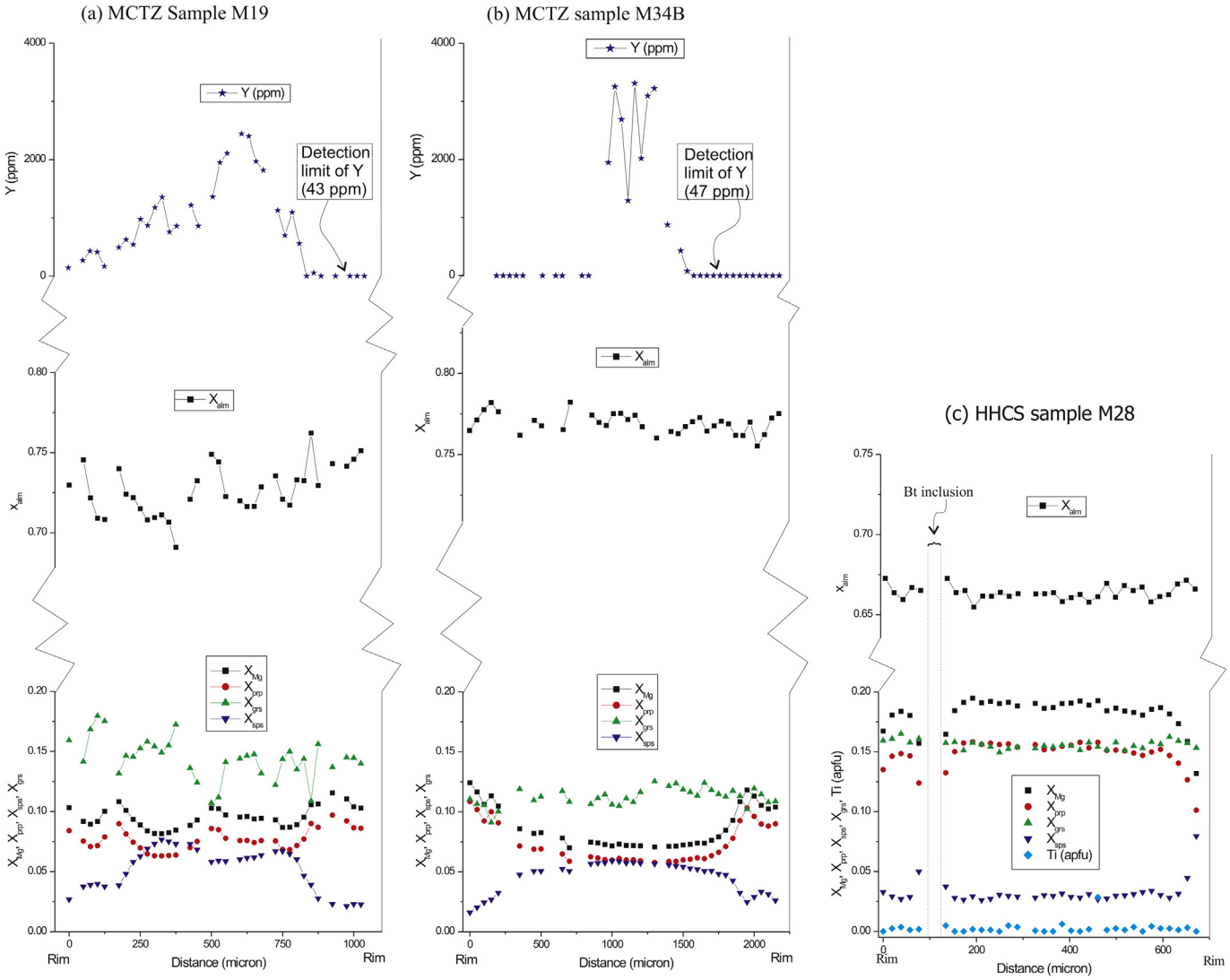

Fig.9. EPMA line scan of zoned garnet porphyroblasts. Discontinuity in the profile is due to inclusions. (a)Garnet porphyroblast from MCTZ sample M19 showing decreasing X_{sps} balanced by increase in X_{prp} from core to rim, while X_{alm} and X_{prp} show minor fluctuations. Y content decreases from core to rim; (b)Garnet porphyroblast from MCTZ sample M34b showing decreasing X_{sps} and increasing X_{prp} from core to rim, while X_{grs} and X_{alm} are almost uniform. Note sharp decrease in Y from core to rim; (c)Garnet porphyroblast from HHCS sample M28 showing uniform composition except near a biotite inclusion and at the outermost rim, where X_{sps} increases and X_{prp} decreases sharply. Ti content (apfu) remains uniform. Abbreviations: $X_{Mg} = Mg/(Mg + Fe)$; $X_{alm} = Fe/(Fe + Mg + Ca + Mn)$; $X_{prp} = Mg/(Fe + Mg + Ca + Mn)$; $X_{grs} = Ca/(Fe + Mg + Ca + Mn)$ and $X_{sps} = Mn/(Fe + Mg + Ca + Mn)$.

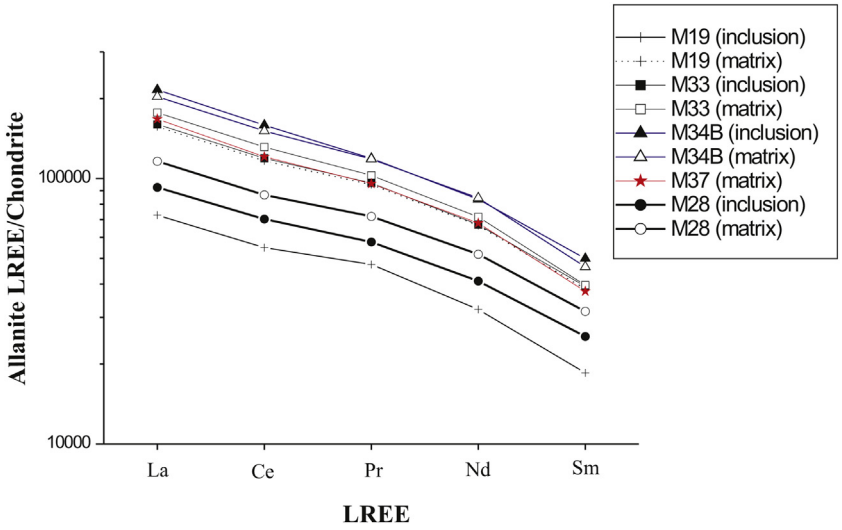

Fig.10. Chondrite-normalised LREE plot for allanite inclusions in garnet and matrix allanites from MCTZ samples M37, M19, M34B, M33, and HHCS sample M28. Chondrite data for normalisation from McDonough and Sun (1995).

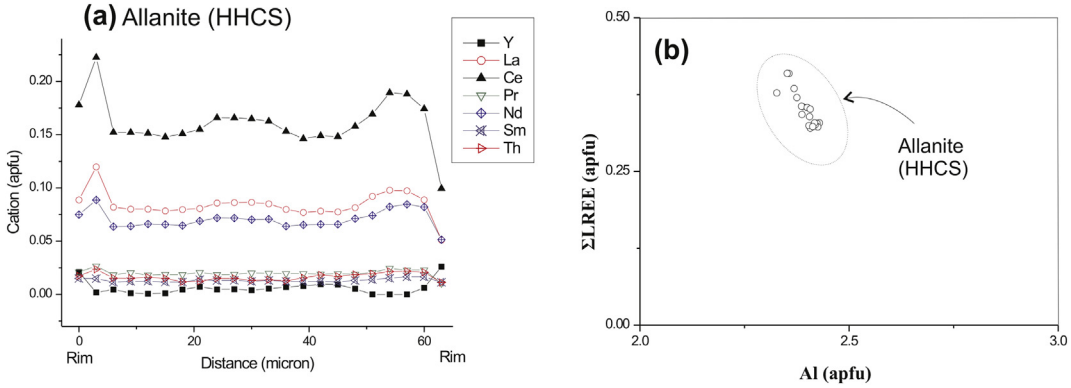

Fig.11. (a)Line scan along A–B in Fig.8e showing oscillatory variation in La, Ce, Pr, Nd, Sm, Th and Y in allanite from HHCS sample M28; (b)Al vs ΣLREE plot for line scan data presented in (a).

porphyroblasts in the MCTZ samples M19, M34B and M33 contain allanite inclusion in the rim but not in the core which implies that allanite became a stable phase after the growth of the Y-rich core. Allanite sequestered available Y during the formation of the garnet rim and therefore the latter was depleted in Y. An alternative explanation for the narrow Y-rich core is that Y partitions more strongly into garnet than the major elements, with little Y available after the growth of the Y-rich core.

The development of a high-Y annulus in a relatively inclusion-free zone of garnet rim in the MCTZ sample M37 is a particularly interesting feature in the present sample suite (Fig.5d). Such annuli in garnet are generally known from staurolite or higher grade metapelites (Pyle and Spear, 1999; Yang and Pattison, 2006). On the other hand, M37 is a garnet grade metapelite from the lowest structural level of the MCTZ. Several possible mechanisms for annular rings of high Y in garnet have been proposed by Lanzirotti (1995) including (1)changes in garnet growth rates (our preferred mechanism); (2)breakdown of Y-enriched phases; and (3)garnet resorption and renewed growth. The M37 garnet lacks textural evidence of resorption. There is no microtextural evidence of breakdown of Y-enriched phases such as allanite or monazite in the sample. The presence of Y annulus in a relatively inclusion-free zone of garnet rim can be explained by a decrease in the growth rate of the crystal (Lanzirotti, 1995; Yang and Rivers, 2002; Yang and Pattison, 2006).

Table8
Bulk compositions of MCTZ and HHCS rocks (oxides in wt%, elements in ppm).

	MCTZ				HHCS	
	M37	M19B	M34B	M33	M28	HH52
SiO_2	56.52	59.68	61.03	54.33	59.62	58.66
TiO_2	0.68	0.78	0.79	0.85	0.89	0.79
Al_2O_3	20.56	19.78	21.59	23.21	18.66	17.74
FeO	7.30	6.22	5.88	7.71	8.02	7.80
MnO	0.05	0.07	0.08	0.11	0.09	0.09
MgO	3.56	2.39	1.73	2.56	2.37	4.06
CaO	0.83	1.06	0.49	0.57	0.84	1.68
Na_2O	2.43	2.13	1.16	1.01	1.16	2.09
K_2O	3.60	3.75	4.61	5.67	5.29	3.63
P_2O_5	0.13	0.13	0.14	0.20	0.41	0.26
LOI	2.43	2.09	2.34	2.65	0.99	1.24
Cr	275	251	272	227	226	320
Cu	126	41	9	17	26	42
Zn	351	110	39	98	83	64
Y	27	27	26	27	30	29
Zr	169	204	211	242	225	137
Nb	14	17	19	17	16	10
Th	20	16	17	20	18	15
Total	98.19	98.15	99.90	98.93	98.40	98.04

Garnet porphyroblasts from the HHCS sample M28 show weak Y zoning with slight increase in its concentration at the rim (Figs.5e–f). These garnets are marked by textural evidence of resorption in parts of the rim (Figs.5e–f) and a sharp increase in Mn towards the outermost part of the rim (Figs.7d, 9c). These features taken together suggest that the likely cause of Y and Mn zoning is localised resorption of the crystal and back-diffusion of these elements. When garnet resorbs, Y and Mn still partition favourably into garnet, thereby reincorporating into the crystal rim by diffusion (Lanzirotti, 1995).

7.4. Y zoned garnets from other parts of the Himalaya

In the study of an MCTZ pelitic schist of staurolite grade (600–640 °C, 7.0–7.3 kbar) from the Sutlej Valley, NW Himalaya, Caddick et al. (2007) reported garnet zoning marked by a wide core of uniform Y content and a thin, Y-poor rim. The Y zoning was interpreted to result from either a hiatus in crystal growth (the rim growing under different *P–T* conditions than the core) or continual growth during which an additional Y-bearing phase sequestered available Y. Langille et al. (2012) reported garnet zoning with decreasing Y from the core to the rim in staurolite to kyanite grade pelitic schists (530–630 °C, 6.6–7.6 kbar) from the upper reaches of the Sutlej Valley, but did not offer any explanation for the Y zoning.

In central Nepal, Kohn (2004) documented sector zoning and oscillatory zoning of Y in garnet from MCTZ and HHCS pelitic schists of garnet to kyanite grade and attributed them to crystal growth kinetic effects resulting from extraordinarily rapid, possibly cyclic thrusting. Martin (2009) reported spiral zoning of Y and Cr in garnets from a lower amphibolites facies MCTZ schist (~570 °C, ~9 kbar) from central Nepal and suggested that the garnets preserve Y and Cr heterogeneity in the matrix at the scale of tens of micrometers during breakdown of matrix minerals during garnet growth. Several patterns of Y zoning in garnet from sillimanite grade HHCS gneisses (> 700 °C, ~7 kbar) from east central Nepal were reported by Shrestha et al. (2017) which include: (i)high Y at the core, which initially decreases in the mantle and then increases towards the rim; and (ii) positive bell-shaped profile with a sharp increase at the outermost rim. The authors attributed these patterns to non-equilibrium and/or diachronous growth of garnet and monazite. Wang et al. (2015) also reported Y zoning in garnets from kyanite to sillimanite grade rocks (640–750 °C) from east central Nepal which varied from Y-rich to Y-poor core relative to the rim, but did not offer any explanation for these patterns.

Groppo et al. (2010) documented garnet zoning with an outward increase of Y in the core followed by a sharp decrease towards the rim in a kyanite grade gneiss (~820 °C, ~13 kbar) from the upper portion of the MCTZ in eastern Nepal. Similar Y zoning pattern in garnet was reported by Regis et al. (2014) from sillimanite grade HHCS metapelites

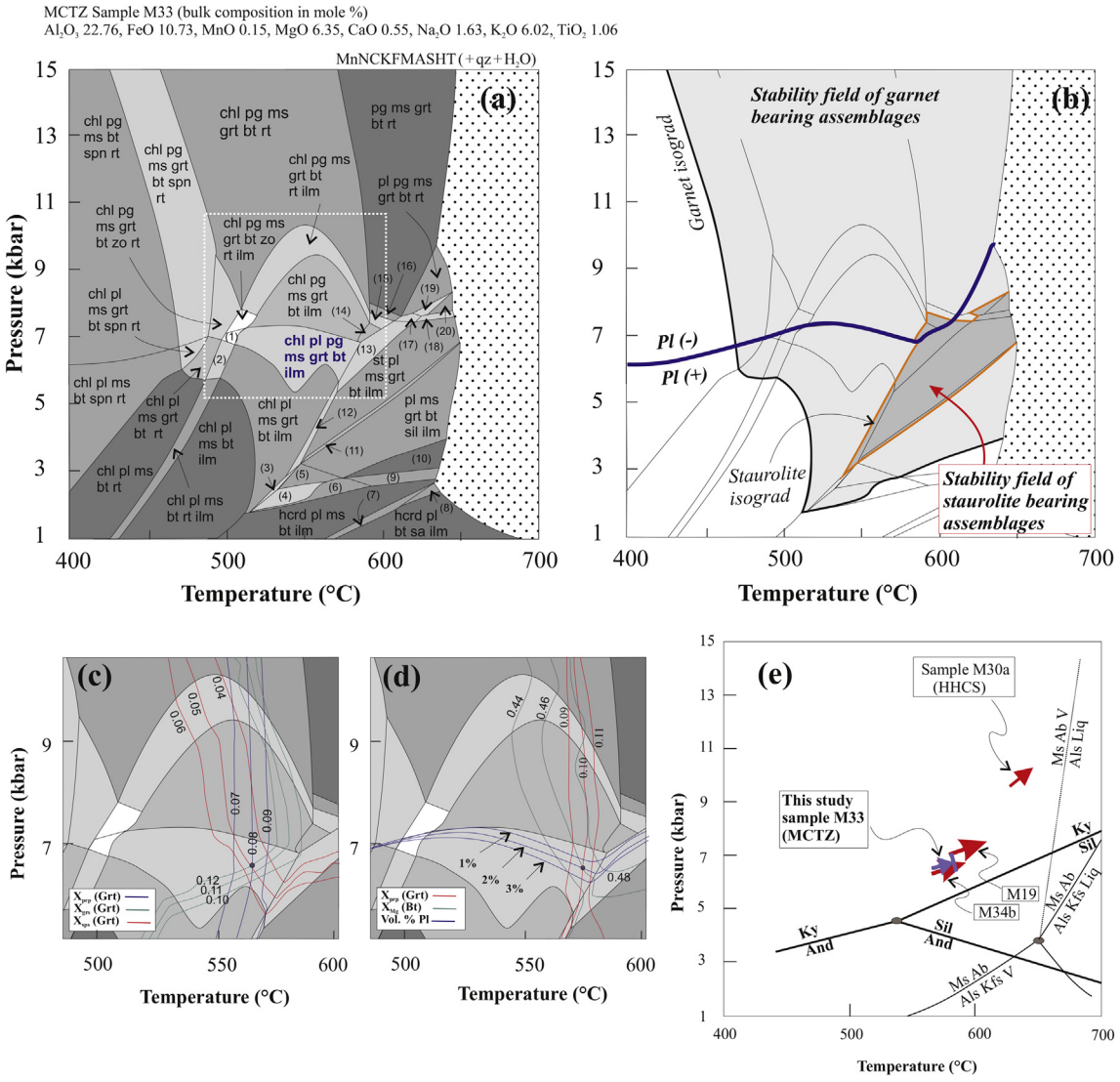

(1) chl pl pg ms grt bt rt ilm
(2) chl pl ms grt bt rt ilm
(3) chl pl ms grt bt and ilm
(4) hcrd pl ms grt bt and ilm
(5) pl ms grt bt and ilm
(6) hcrd pl ms bt and ilm
(7) hcrd pl ms bt sa ilm
(8) hcrd pl bt sil sa ilm
(9) hcrd pl ms bt sil ilm
(10) pl ms bt sil ilm
(11) st pl ms grt bt sil ilm
(12) chl st pl pg ms grt bt ilm
(13) st pl pg ms grt bt ilm
(14) chl st pg ms grt bt ilm
(15) st pg ms grt bt rt ilm
(16) pg ms grt bt rt ilm
(17) pl pg ms grt bt rt ilm
(18) st pl mg grt bt rt ilm
(19) st pl pg ms grt bt rt
(20) st pl ms grt bt rt

Fig.12. Phase diagrams (a–d) constructed for fixed bulk rock composition in the MnNCKFMASHT system (+ qz + H_2O) and *P–T* plot (e)for MCTZ sample M33. (a)Stability field of the assemblage grt–bt–chl–pl–pg–ms–qz is marked in bold letters. The dotted area in the right side of the phase diagram represents melt-bearing assemblages; (b)Stability field of all garnet-bearing assemblages is shown in light grey shade, while that of a staurolite-bearing assemblage is shown in dark grey shade. Note that plagioclase-bearing assemblages are stable at less than ~7.0 kbar pressure; (c)compositional isopleths of X_{prp}, X_{sps} and X_{grs} corresponding to the measured core composition of garnet intersect at *P–T* conditions of 6.5 kbar and 566 °C; (d)compositional isopleths of X_{grs} in garnet rim and X_{Mg} in biotite, and modal abundance of plagioclase intersect at point corresponding to *P–T* conditions of 6.5 kbar and 576 °C; (e)*P–T* path for sample M33; *P–T* paths for samples M19, M34B and M30a are from Thakur et al. (2015).

(~800 °C, ~8.5 kbar) from the Bhutan Himalaya. These patterns led Groppo et al. (2010) and Regis et al. (2014) to propose prograde dissolution of a Y-phase during the formation of the garnet core followed by monazite growth during the formation of the rim. On the other hand, in the study of a sillimanite grade HHCS metapelite from the Bhutan Himalaya, Regis et al. (2016) documented growth of high-Y garnet core in the presence of allanite and xenotime which possibly indicate disequilibrium or diachronous growth of garnet and monazite. Mottram et al. (2015) observed garnet zoning with a Y-rich core and Y-poor rim from kyanite grade MCTZ metapelites (640–680 °C; 8.0–9.0 kbar) from the Sikkim Himalaya, and interpreted it to be due to preferential sequestering of Y to monazite during the formation of the rim.

The above studies from different parts of the Himalaya show that the nature of Y zoning in garnet varies widely depending on local factors. Garnet zoning with Y-rich core and Y-poor rim in the studied MCTZ rocks of garnet grade from the Alaknanda Valley is broadly comparable to that from central Nepal(Wang et al., 2015) and Sikkim Himalaya (Mottram et al., 2015), but the metapelites from those areas are of higher metamorphic grade falling in the kyanite or sillimanite zone. The spiral Y zoning in the M19 garnet core indicates preservation of Y

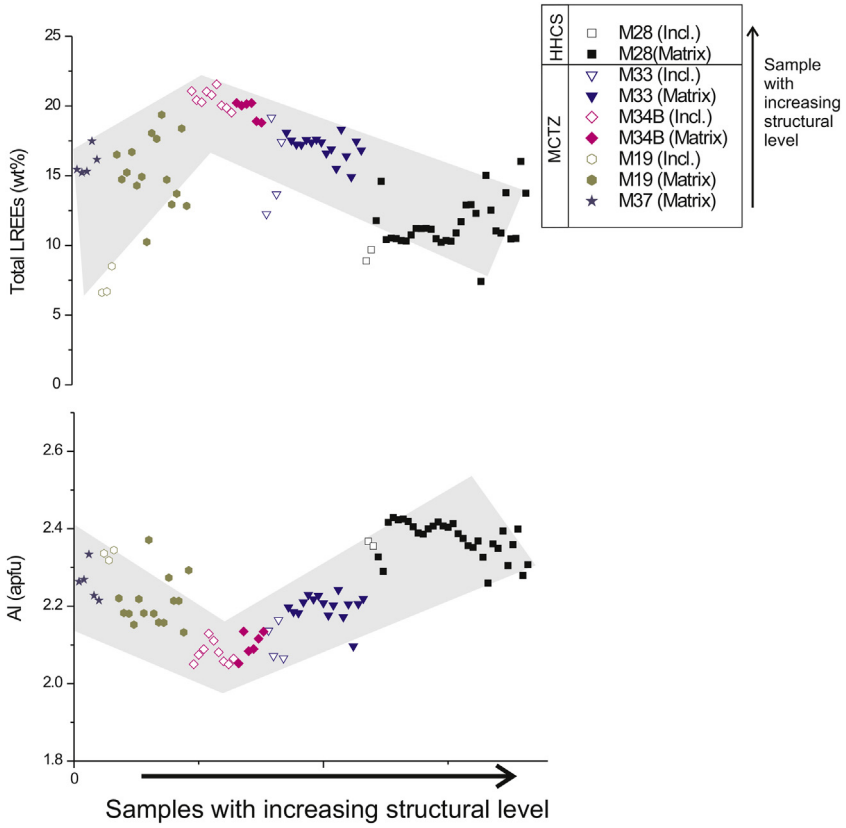

Fig.13. Allanite compositional plot for different samples showing variations in ΣLREE and Al with increasing structural level of the samples along the Alaknanda Valley. Allanites from different samples are represented by different symbols. A symbol with filling is matrix-allanite and without filling is inclusion-allanite. For each of the samples, individual point analyses of allanite have been plotted at a constant spatial interval but without any particular order in the concentration of elements.

heterogeneity in the matrix during the breakdown of matrix minerals during garnet growth (Martin, 2009).

8. Conclusions

Garnet porphyroblasts in garnet grade MCTZ metapelites from the Alaknanda Valley commonly exhibit Y zoning with a Y-rich core and Y-poor rim. Y depletion in the garnet rim is attributed to the sequestration of Y by allanite, which occurs as inclusion in the garnet rim but not in the garnet core in MCTZ rocks. Alternatively, the zoning can be explained by strong partitioning of Y into garnet such that most of it is in the core and there is little Y available towards the later part of garnet growth. High-Y annulus in garnet occurring in a relatively inclusion-free zone of garnet rim is likely to have resulted from a decrease in the growth rate of the crystal. Garnet porphyroblasts in kyanite grade HHCS metapelites occurring immediately above the MCTZ show weak Y zoning with slightly high concentration of Y at the rim which is attributed to localised resorption of the crystal and back-diffusion of Y. The HHCS garnets contain allanite inclusions both in the core and rim which suggest that allanite was a stable phase throughout garnet growth and sequestered available Y. Allanite shows variation in ΣLREE content and complementary variation in Al which appear to be linked to the modal abundance of garnet in different rocks.

Supplementary data to this article can be found online at https://doi.org/10.1016/j.lithos.2018.09.002.

Acknowledgements

The paper is the outcome of research on the Himalayan orogen funded by the Wadia Institute of Himalayan Geology, Dehradun, India under the Institute project code TAT 1.8. We thank Dr. Meera Tiwari, Director of the Institute for providing instrument facility and kind permission to publish the article. We thank Macro Scambelluri for editorial handling. Two anonymous reviewers are thanked for their highly constructive comments on earlier versions of the manuscript. We thank D. Pattison and an anonymous reviewer for their detailed and highly constructive comments on the present version of the manuscript which helped us to improve the quality of the manuscript. The CSIR, New Delhi is acknowledged for providing a fellowship to S. Pandey. The DST, Govt. of India is thanked for funding the EPMA National Facility at IIT Bombay under the IRPHA project code IR/S4/ESF-16/2009 (G). We thank Dr. N.K. Saini and Mr. Chandrashekhar for XRF analysis.

References

Ancey, M., Bastenaire, F., Tixier, R., 1978. Applications of statistical methods in microanalysis. In: Maurice, F., Meny, L., Tixier, R. (Eds.), Microanalysis and Scanning Electron Microscopy. Les Editions De Physique, France, pp. 319–343.

Arita, K., 1983. Origin of the inverted metamorphism of the lower Himalayas, Central Nepal. Tectonophysics 93, 43–60.

Baxter, E.F., Caddick, M.J., Dragovic, B., 2017. Garnet: a rock-forming mineral petrochronometer. Rev. Mineral. Petrol. 83, 469–533.

Budzyn, B., Harlov, D.E., Kozub-Budzyn, G.A., Majka, J., 2017. Experimental constraints on the relative stabilities of the two systems monazite-(Ce) –allanite-(Ce) – fluorapatite and xenotime-(Y)– (Y,HREE)-rich epidote – (Y,HREE)-rich fluorapatite, in high Ca and Na-Ca environments under P-T conditions of 200–1000 MPa and 450–570°C. Mineral. Petrol. 111, 183–217.

Caddick, M.J., Bickle, M.J., Harris, N.B.W., Holland, T.J.B., Horstwood, M.S.A., Parrish, R.R., Ahmad, T., 2007. Burial and exhumation history of a Lesser Himalayan schist: Recording the formation of an inverted metamorphic sequence in NWIndia. Earth Planet. Sci. Lett. 264, 375–390.

Caddick, M.J., Konopasek, J., Thompson, A.B., 2010. Preservation of garnet growth zoning and the duration of prograde metamorphism. J. Petrol. 51, 2327–2347.

Catlos, E., Harrison, T.M., Kohn, M.J., Grove, M., Lovera, O.M., Ryerson, F.J., Upreti, B.N., 2001. Geochronological and thermobarometric constraints on the evolution of the

Main Central Thrust, central Nepal Himalaya. J. Geophys. Res. 106, 16177–16203.
Catlos, E.J., Gilley, L.D., Harrison, T.M., 2002. Interpretation of monazite ages obtained via in situ analysis. Chem. Geol. 188, 193–215.
Celerier, J., Harrison, T.M., Beyssac, O., Herman, F.M., Dunlap, W.J., Webb, A.A., 2009. The Kumaon and Garhwal Lesser Himalaya, India: part 2. Thermal and deformation histories. Bull. Geol. Soc. Am. 121, 1281–1297.
Chatterjee, N.D., Froese, E., 1975. A thermodynamic study of the pseudo–binary join muscovite–paragonite in the system $KAlSi_3O_8$–$NaAlSi_3O_8$–Al_2O_3–H_2O. Am. Mineral. 60, 985–993.
Connolly, J.A.D., 2005. Computation of phase equilibria by linear programming: a tool from geodynamic modelling and its application to subduction zone decarbonation. Earth Planet. Sci. Lett. 236, 524–541.
Connolly, J.A.D., Kerrick, D.M., 2002. Metamorphic controls on seismic velocity of subducted oceanic crust at 100–250 km depth. Earth Planet. Sci. Lett. 204, 61–75.
Corrie, S.L., Kohn, M.J., 2008. Trace-element distributions in silicates during prograde metamorphic reactions: implications for monazite formation. J. Metamorph. Geol. 26, 451–464.
Cruz-Uribe, A.M., Hoisch, T.D., Wells, M.L., Vervoort, J.D., Mazdab, F.K., 2015. Linking thermodynamic modelling, Lu–Hf geochronology and trace elements in garnet: new *P–T–t* paths from the Sevier hinterland. J. Metamorph. Geol. 33, 763–781.
Deer, W.A., Howie, R.A., Zussman, J., 1986. Rock Forming Minerals. 1B. Disilicates and Ring Silicates. 2nd ed. John Wiley & Sons, New York.
Diener, J.F.A., Powell, R., 2010. Influence of ferric iron on the stability of mineral assemblage. J. Metamorph. Geol. 28, 599–613.
Dragovic, B., Guevara, V.E., Caddick, M.J., Baxter, E.F., Kylander-Clark, A.R.C., 2016. A pulse of cryptic granulite-facies metamorphism in the Archean Wyoming Craton revealed by Sm–Nd garnet and U–Pb monazite geochronology. Precambrian Res. 283, 24–49.
Engi, M., 2017. Petrochronology based on REE-minerals: monazite, allanite, xenotime, apatite. Rev. Mineral. Geochem. 83, 365–418.
Ferry, J.M., 2000. Patterns of mineral occurrence in metamorphic rocks. Am. Mineral. 85, 1573–1588.
Finger, F., Krenn, E., Schulz, B., Harlov, D., Schiller, D., 2016. "Satellite monazites" in polymetamorphic basement rocks of the Alps: their origin and petrological significance. Am. Mineral. 101, 1094–1103.
Fraser, G.L., Pattison, D.R.M., Heaman, L.M., 2004. Age of the Ballachulish and Glencoe Igneous Complexes (Scottish Highlands), and paragenesis of zircon, monazite and baddeleyite in the Ballachulish Aureole. J. Geol. Soc. Lond. 161, 447–462.
Gansser, A., 1964. The Geology of the Himalaya. Willey, New York 289p.
Gasser, D., Bruand, E., Rubatto, D., Stüwe, K., 2012. The behaviour of monazite from greenschist facies phyllites to anatectic gneisses: an example from the Chugach Metamorphic complex, southern Alaska. Lithos 134, 108–122.
Goswami-Banerjee, S., Robyr, M., 2015. Pressure and temperature conditions for crystallization of metamorphic allanite and monazite in metapelites: a case study from the Miyar Valley (high Himalayan Crystalline of Zanskar, NWIndia). J. Metamorph. Geol. 33:535–556. https://doi.org/10.1111/jmg.12133.
Groppo, C., Rolfo, F., Lombardo, B., 2009. P–T evolution across the Main Central Thrust Zone (Eastern Nepal): hidden discontinuities revealed by petrology. J. Petrol. 50, 1149–1180.
Groppo, C., Rubatto, D., Rolfo, F., Lombardo, B., 2010. Early Oligocene partial melting in the Main Central Thrust Zone (Arun valley, eastern Nepal Himalaya). Lithos 118, 287–301.
Gururajan, N.S., Choudhuri, B.K., 1999. Ductile thrusting, metamorphism and normal faulting in Dhauliganga Valley, Garhwal Himalaya. Himalayan Geol. 20, 19–29.
Heinrich, W., Andrehs, G., Franz, G., 1997. Monazite-xenotime miscibility gap thermometry. I. an empirical calibration. J. Metamorph. Geol. 15, 3–16.
Hermann, J., Rubatto, D., 2003. Relating zircon and monazite domains to garnet growth zones: age and duration of granulite facies metamorphism in the Val Malenco lower crust. J. Metamorph. Geol. 21, 833–852.
Hickmott, D.D., Spear, F.S., 1992. Major- and trace-element zoning in garnets from calcareous pelites in the NW Shelburne Falls quadrangle, Massachusetts: garnet growth histories in retrograded rocks. J. Petrol. 33, 965–1005.
Hodges, K.V., 2000. Tectonics of the Himalaya and southern Tibet from two perspectives. Geol. Soc. Am. Bull. 112, 324–350.
Hodges, K.V., Silverberg, D.S., 1988. Thermal evolution of the Greater Himalaya, Garhwal, India. Tectonics 7, 583–600.
Holland, T.J.B., Powell, R., 1998. An internally consistent thermodynamic dataset for phases of petrological interest. J. Metamorph. Geol. 16, 309–344.
Holland, T., Powell, R., 2003. Activity–composition relations for phases in petrological calculations: an asymmetric multicomponent formulation. Contrib. Mineral. Petrol. 145, 492–501.
Holland, T., Baker, J., Powell, R., 1998. Mixing properties and activity–composition relationships of chlorites in the system MgO–FeO–Al2O3–SiO2–H2O. Eur. J. Mineral. 10, 395–406.
Hollister, L.S., 1966. Garnet zoning: an interpretation based on the Rayleigh fractionation model. Science 154, 1647–1651.
Janots, E., Engi, M., Berger, A., 2006. Evolution of REE minerals from diagenetic to amphibolite facies conditions in the Central Alps, with implications to geochronology. Geochim. Cosmochim. Acta 70, A290.
Janots, E., Brunet, F., Goffe, B., Poinssot, C., Burchard, M., Cemic, L., 2007. Thermochemistry of monazite-(La) and dissakisite-(La): implications for monazite and allanite stability in metapelites. Contrib. Mineral. Petrol. 154, 1–14.
Janots, E., Engi, M., Berger, A., Allaz, J., Schwarz, J.O., Spandler, C., 2008. Prograde metamorphic sequence of REE minerals in pelitic rocks of the Central Alps: implications for allanite-monazite-xenotime phase relations from 250 to 610°C. J. Metamorph. Geol. 26, 509–526.
Kohn, M.J., 2004. Oscillatory- and sector-zoned garnets record cyclic (?) rapid thrusting in Central Nepal. Geochem. Geophys. Geosyst. 5, 1–9.
Kohn, M.J., 2014. Himalayan metamorphism and its tectonic implications. Annu. Rev. Earth Planet. Sci. 42, 381–419.
Kohn, M.J., Malloy, M.A., 2004. Formation of monazite via prograde metamorphic reactions among common silicates: implications for age determinations. Geochim. Cosmochim. Acta 68, 101–113.
Kohn, M.J., Catlos, E.J., Ryerson, F.J., Harrison, T.M., 2001. Pressure-temperature-time pathdiscontinuity in the Main Central thrust zone, Central Nepal. Geology 29, 571–574.
Konrad-Schmolke, M., Zack, T., O'Brien, P.J., Jacob, D.E., 2008. Combined thermodynamic and rare earth element modeling of garnet growth during subduction: examples from ultrahigh-pressure eclogite of the Western Gneiss Region, Norway. Earth Planet. Sci. Lett. 272, 488–498.
Krenn, E., Finger, F., 2007. Formation of monazite and rhabdophane at the expense of allanite during Alpine low temperature retrogression of metapelitic basement rocks from Crete, Greece: microprobe data and geochronological implications. Lithos 95, 130–147.
Krenn, E., Ustaszewski, K., Finger, F., 2008. Detrital and newly formed metamorphic monazite in amphibolite-facies metapelites from the Motajica Massif, Bosnia. Chem. Geol. 254, 164–174.
Langille, J.M., Jessup, M.J., Cottle, J.M., Lederer, G., Ahmad, T., 2012. Timing of metamorphism, melting and exhumation of the Leo Pargil dome, Northwest India. J. Metamorph. Geol. 30, 769–791.
Lanzirotti, A., 1995. Yttrium zoning in metamorphic garnets. Geochim. Cosmochim. Acta 59, 4105–4110.
Lefort, P., 1975. Himalayas, the collided range: present knowledge of the continental arc. Am. J. Sci. 275, 1–44.
Martin, A.J., 2009. Sub-millimeter heterogeneity of yttrium and chromium during growth of semi-pelitic garnet. J. Petrol. 50, 1713–1727.
McDonough, W.F., Sun, S.S., 1995. The Composition of the Earth. Chem. Geol. 120, 223–253.
Merlet, C., 1992. Electron Probe Microanalysis: New accurate Φ (ρz) description. Electron Microbeam Anal. 12, 107–115.
Moharana, A., Mishra, A., Srivastava, D.C., 2013. Deformation style in the Munsiari Thrust Zone: a study in the Madlakia–Munsiari–Dhapa section in north-eastern Kumaun Himalaya. Int. J. Earth Sci. 102, 1837–1849.
Moore, S.J., Carlson, W.D., Hess, M.A., 2013. Origins of yttrium and rare earth element distributions in metamorphic garnet. J. Metamorph. Geol. 31, 663–689.
Mottram, C.M., Parrish, R.R., Regis, D., Warren, C.J., Argles, T.W., Harris, N.B.W., Roberts, N. M.W., 2015. Using U–Th–Pb petrochronology to determine rates of ductile thrusting: Time windows into the Main Central Thrust, Sikkim Himalaya. Tectonics 34. https://doi.org/10.1002/2014TC003743.
Newton, R.C., Charlu, T.V., Kleppa, O.J., 1980. Thermochemistry of the high structural state plagioclases. Geochim. Cosmochim. Acta 44, 933–941.
Otamendi, J.E., de la Rosa, J.D., Patino Douce, A.E., Castro, A., 2002. Rayleigh fractionation of heavy rare earths and yttrium during metamorphic garnet growth. Geology 30, 159–162.
Palin, R.M., Weller, O.M., Waters, D.J., Dyck, B., 2016. Quantifying geological uncertainty in metamorphic phase equilibria modelling; a Monte Carlo assessment and implications for tectonic interpretations. Geosci. Front. 7, 591–607.
Pattison, D.R.M., De Capitani, C., Gaidies, F., 2011. Petrological consequences of variations in metamorphic reaction affinity. J. Metamorph. Geol. 29, 953–977.
Pouchon, J.L., Pichoir, F., 1984. A new model for the quantitative X-ray analysis, Part–I. Application to the analysis of homogeneous samples. La Recherche Aerospatiale 3, 13–38.
Powell, R., Holland, T., 1999. Relating formulations of the thermodynamics of mineral solid solutions: activity modelling of pyroxenes, amphiboles, and micas. Am. Mineral. 84, 1–14.
Pyle, J.M., Spear, F.S., 1999. Yttrium zoning in garnet: Coupling of major and accessory phases during metamorphic reactions. Geol. Mater. Res. 1, 1–49.
Pyle, J.M., Spear, F.S., 2003. Four generations of accessory-phase growth in low-pressure migmatites from the SW New Hampshire. Am. Mineral. 88, 338–351.
Rasmussen, B., Muhling, J.R., Fletcher, I.R., Wingate, M.T.D., 2006. In situ SHRIMPU-Pb dating of monazite integrated with petrology and textures: does bulk composition control whether monazite forms in low-Ca pelitic rocks during amphibolite facies metamorphism? Geochim. Cosmochim. Acta 70, 3040–3058.
Regis, D., Warren, C.J., Young, D., Roberts, N.M.W., 2014. Tectono-metamorphic evolution of the Jomolhari massif: Variations in timing of syn-collisional metamorphism across western Bhutan. Lithos 190, 449–466.
Regis, D., Warren, C.J., Mottram, C.M., Roberts, N.M.W., 2016. Using monazite and zircon petrochronology to constrain the P–T–t evolution of the middle crust in the Bhutan Himalaya. J. Metamorph. Geol. 34, 617–639.
Robinson, D.M., DeCelles, P.G., Garzione, C.N., Pearson, O.N., Harrison, T.M., Catlos, E.J., 2003. Kinematic model for the Main Central thrust in Nepal. Geology 31, 359–362.
Searle, M.P., Law, R.D., Godin, L., Larson, K.P., Streule, M.J., Cottle, J.M., Jessup, M.J., 2008. Defining the Himalayan Main Central Thrust in Nepal. J. Geol. Soc. Lond. 165, 523–534.
Shaw, D.M., 1956. Geochemistry of pellitic rocks. Part III: major elements and general geochemistry. Bull. Geol. Soc. Am. 67, 919–934.
Shrestha, S., Larson, K.P., Guilmette, C., Smit, M.A., 2017. The P–T–t evolution of the exhumed Himalayan metamorphic core in the Likhu Khola region, East Central Nepal. J. Metamorph. Geol. 35, 663–693.
Skora, S., Baumgartner, L.P., Mahlen, N.J., Johnson, C.M., Pilet, S., Hellebrand, E., 2006. Diffusion-limitedREE uptake by eclogite garnets and its consequences for Lu–Hf and Sm–Nd geochronology. Contrib. Mineral. Petrol. 152, 703–720.
Smith, H.A., Barreiro, B., 1990. Monazite U–Pb dating of staurolite grade metamorphism in pelitic schists. Contrib. Mineral. Petrol. 105, 602–615.

Spear, F.S., 2010. Monazite–allanite phase relations in metapelites. Chem. Geol. 279, 55–62.
Spear, F.S., Kohn, M.J., 1996. Trace element zoning in garnet as a monitor of crustal melting. Geology 24, 1099–1102.
Spear, F.S., Thomas, J.B., Hallett, B.W., 2014. Overstepping the garnet isograd: a comparison of QuiG barometry and thermodynamic modelling. Contrib. Mineral. Petrol. 168, 1059 (https://doi.org/10.1007/s00410-1059-6https://doi.org/10.1007/s00410-1059-6.
Spencer, C.J., Harris, R.A., Dorais, M.J., 2012. The metamorphism and exhumation of the Himalayan metamorphic core, eastern Garhwal region, India. Tectonics 31. https://doi.org/10.1029/2010TC002853 TC1007.
Suzuki, K., Adachi, M., 1994. Middle Precambrian detrital monazite and zircon from the Hida gneiss on Oki-Dogo Island, Japan: their origin and implications for the correlation of basement gneiss of Southwest Japan and Korea. Tectonophysics 235, 277–292.
Thakur, S.S., Patel, S.C., Singh, A.K., 2015. A P–T pseudosection modelling approach to understand metamorphic evolution of the Main Central Thrust Zone in the Alaknanda valley, NW Himalaya. Contrib. Mineral. Petrol. 170 (2). https://doi.org/10.1007/s00410-015-1159-y.
Thompson, J.B., Hovis, G.L., 1979. Entropy of mixing in sanidine. Am. Mineral. 64, 57–65.
Tomkins, H.S., Pattison, D.R.M., 2007. Accessory phase petrogenesis in relation to major phase assemblages in pelites from the Nelson contact aureole, southern British Columbia. J. Metamorph. Geol. 25, 401–421.
Townsend, K.J., Miller, C.F., D'Andrea, J.L., Ayers, J.C., Harrison, T.M., Coath, C.D., 2000. Low temperature replacement of monazite in the Ireteba Granite, southern Nevada, geochronological implications. Chem. Geol. 172, 95–112.
Valdiya, K.S., 1980. The two intracrustal boundary thrusts of the Himalaya. Tectonophysics 66, 323–348.
Wang, J., Rubatto, D., Zhang, J., 2015. Timing of partial melting and cooling across the Greater Himalayan Crystalline Complex (Nyalam, Central Himalaya): In-sequence thrusting and its implications. J. Petrol. 56, 1677–1702.
White, R.W., Powell, R., Holland, T.J.B., 2001. Calculation of partial melting equilibria in the system Na_2O–CaO–K_2O–FeO–MgO–Al_2O_3–SiO_2–H_2O (NCKFMASH). J. Metamorph. Geol. 19, 139–153.
Whitney, D.L., Evans, B.W., 2010. Abbreviations for names of rock-forming minerals. Am. Mineral. 95, 185–587.
Wing, B., Ferry, J., Harrison, T.M., 2003. Prograde destruction and formation of monazite and allanite during contact and regional metamorphism of pelites: petrology and geochronology. Contrib. Mineral. Petrol. 145, 228–250.
Yakymchuk, C., Clark, C., White, R.W., 2017. Phase relations, reaction sequences and petrochronology. Rev. Mineral. Geochem. 83, 13–53.
Yang, P., Pattison, D., 2006. Genesis of monazite and Y zoning in garnet from the Black Hills, South Dakota. Lithos 88, 233–253.
Yang, P., Rivers, T., 2002. The origin of Mn and Y annuli in garnet and the thermal dependence of P in garnet and Y in apatite in calc-pelite and pelite, Gagnon terrane, western Labrador, western Labrador. Geol. Mater. Res. 4, 1–35.
Yin, A., 2006. Cenozoic tectonic evolution of the Himalayan orogen as constrained by along-strike variation of the structural geometry, exhumation history, and foreland sedimentation. Earth Sci. Rev. 76, 1–131.